AGU PUBLICATIONS

JGR

Journal of Geophysical Research: Solid Earth

RESEARCH ARTICLE
10.1002/2017JB013928

Key Points:
- Large surface displacements related to a low-magnitude shallow earthquake
- Low rigidity medium possibly associated with postseimic activity reconciles observations
- Illustration of unusual processes is revealed by systematic InSAR analyses

Supporting Information:
- Supporting Information S1
- Table S1
- Figure S1
- Figure S2
- Figure S3
- Figure S4
- Figure S5

Correspondence to:
J. Champenois,
champenoisjohann@gmail.com

Citation:
Champenois, J., Baize, S., Vallee, M., Jomard, H., Alvarado, A. P., Espin, P., ... Audin, L. (2017). Evidences of surface rupture associated with a low-magnitude (M_w5.0) shallow earthquake in the Ecuadorian Andes. *Journal of Geophysical Research: Solid Earth*, *122*. https://doi.org/10.1002/2017JB013928

Received 2 JAN 2017
Accepted 1 SEP 2017
Accepted article online 9 SEP 2017

Evidences of Surface Rupture Associated With a Low-Magnitude (M_w5.0) Shallow Earthquake in the Ecuadorian Andes

J. Champenois[1], S. Baize[1], M. Vallee[2], H. Jomard[1], A. Alvarado[3], P. Espin[3], G. Ekström[4], and L. Audin[5]

[1]Seismic Hazard Division, Institut de Radioprotection et de Sûreté Nucléaire, Fontenay-aux-Roses, France, [2]Institut de Physique du Globe de Paris UMR 7154, Paris, France, [3]Instituto Geofisico, Escuela Politecnica Nacional, Quito, Ecuador, [4]Department of Earth and Environmental Sciences, Columbia University, New York, NY, USA, [5]Institut des Sciences de la Terre UMR 5275, Grenoble, France

Abstract This study analyzes surface displacements generated by a low-magnitude crustal earthquake in the Ecuadorian Andes by combining analysis of synthetic aperture radar (SAR) interferometry, geological field investigations, and seismological data. In March 2010, a significant surface faulting event occurred in the Pisayambo area (Eastern Cordillera), along the major dextral fault zone bounding the North Andean Sliver and the South America Plate. Interferograms were inverted to determine fault plane geometry and slip displacement distribution. The event affected a 9 km long previously unknown fault, referred as the Laguna Pisayambo Fault, with purely dextral movement reaching 45 cm and concentrated in the top 3 km of the crust. Geological investigations confirm both the fault mechanism and the amplitude of displacements. While these large displacements would be related to an event with a magnitude of 5.44 if using a standard crustal rigidity, we show that they can be convincingly associated with an M_w5.0 earthquake, that occurred on 26 March 2010. Reconciling the apparent differences in magnitude requires the existence of a low-rigidity medium at shallow depths and/or postseismic activity of the fault. However, considering only the latter hypothesis would imply an unusually active postseismic process, in which 400–500% of the coseismic moment is released in the 6 days following the earthquake. Our observations highlight that the scaling laws relating surface observations to earthquake magnitude, classically used for seismic hazard assessment, should be carefully used. This study also illustrates how systematic InSAR analysis, even in places where no clues of ground deformation are present, can reveal tectonic processes.

1. Introduction

The Ecuador seismotectonics is dominated by the subduction of the Nazca plate beneath the South America Plate, at a velocity of 5.6 cm/yr. Most of this convergence is occurring below the coast on the subduction interface, but a significant remaining part is accommodated by the 7–9 mm/yr northeast motion of the North Andean Sliver (NAS) with respect to the South America Plate (Nocquet et al., 2014; Pennington, 1981) (Figure 1a). This internal deformation is located in the Central Andes, in a narrow zone of distributed deformation referred as the Chingual-Cosanga-Puna-Pallatanga (CCPP) fault system, that runs north from the Gulf of Guayaquil toward the Carribean sea. Large and destructive crustal earthquakes have occurred in this area (Beauval et al., 2010), the best known being the 1797 Riobamba and 1949 Ambato events. The CCPP fault segments are included as important earthquake sources for seismic hazard analyses (Yepes et al., 2016).

A large-scale mapping of the potential active segments of the CCPP has been recently proposed (Alvarado, 2012) and a first paleoseismological study has been carried out along the Pallatanga segment, pointing out evidences of several large (*M*7+) paleoearthquakes (Baize et al., 2015). Besides classical field mapping of fault segments based on geomorphological analyses, we performed a systematic interferometric synthetic aperture radar (InSAR) analysis of the Riobamba-Ambato-Latacunga region (Figure 1b). As an unexpected result, a surface displacement event was identified between successive SAR images between March and April 2010 along the CCPP fault system, in the western part of the Cordillera Real, close to the Pisayambo lake. This event occurred within a 16 day time span along an unknown fault segment of the CCPP, hereafter referred to as the Laguna Pisayambo Fault (LPF).

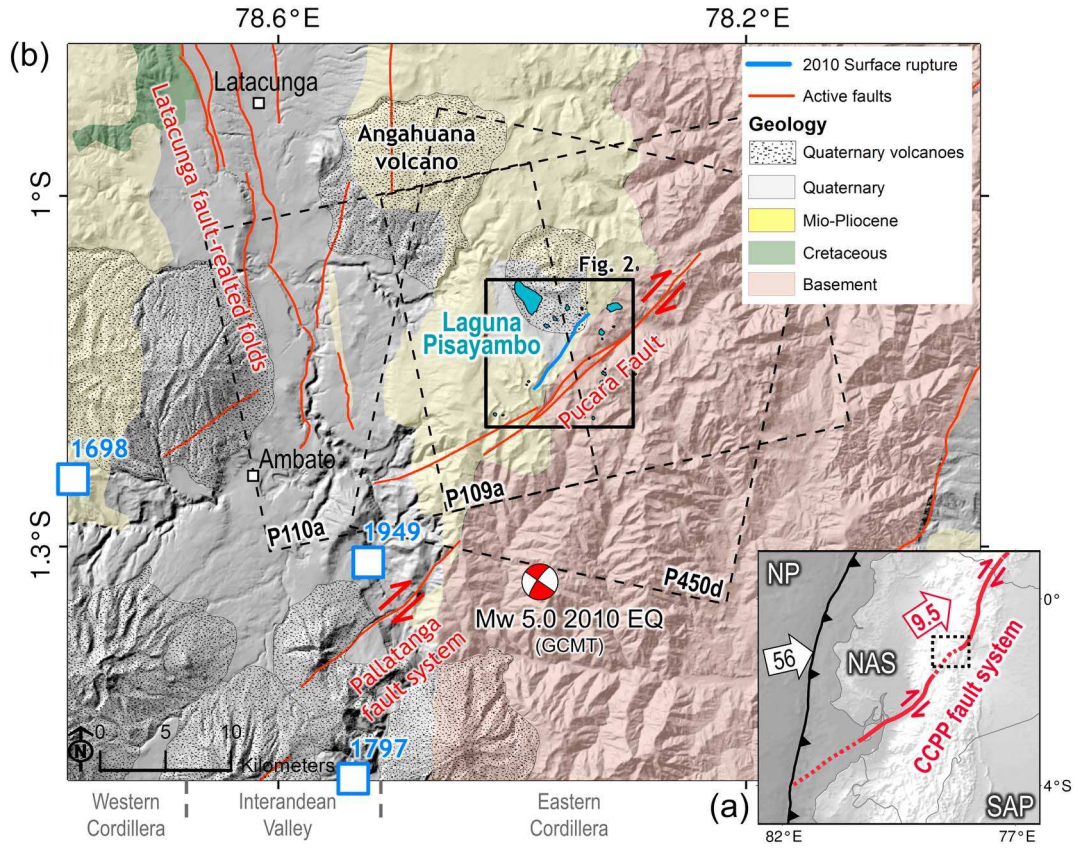

Figure 1. (a) Tectonic setting of Ecuador. The black line shows the location of the trench, related to the subduction of Nazca Plate (NP) beneath the North Andean Sliver (NAS) and the South American Plate (SAP). The red line shows the North Andean Sliver limit, called the Cosanga-Chingual-Pallatanga-Puna (CCPP) fault system. Arrows indicate the motion of the NP and NAS with respect to the SAP. Velocities are expressed in mm/yr. The black dashed rectangle shows the location of the Pisayambo region presented in Figure 1b. (b) Topographic and tectonic map of the Pisayambo area. Red lines represent major faults (Alvarado, 2012), while blue line represents the 2010 surface rupture. Black dashed lines delimit the imprint of the radar frames used in this study. Black box shows the location of the InSAR study area presented in Figure 2. Blue squares show locations of large historical earthquakes.

The studied area is characterized by a high-elevation plateau (>3,500 m above sea level, asl), overhanging the Interandean Valley (2,500–3,000 m asl). To the northeastern rim of the Pisayambo lake, the Angarahua caldera relief is rising up to 4,000 m above sea level, and the mountains flanking the LPF to the south-southeast reach a similar elevation. The surface geology of the study area includes Mio-Pliocene sediments and volcanic rocks (Pisayambo Formation), as well as Quaternary series that cover tectonic slices of basement rocks (intrusive, volcanic, and sedimentary series of Triassic to Jurassic ages) (Figure 1b). The most recent series are deposits associated with the Pleistocene Angahuana caldera, Upper Pleistocene to Holocene glacial layers, and thick black soils (andisols).

The LPF is located 4 km southeast of the Pisayambo lake, upstream of an artificial dam and its hydroelectrical facility (76 MW; megawatt) and extends over 9 km in a roughly NE-SW direction. The LPF, as it can be inferred from the geodetical and geological results presented hereafter, appears to develop slightly (2.5 km) north of the closest CCPP segment (Pucara fault, Figure 1b) as previously mapped by Alvarado (2012). To check and further document these observations, we combine the detailed analysis of the InSAR images with a geological field survey and seismological investigations.

2. InSAR Analysis

2.1. SAR Data and Interferograms

This study uses PALSAR (Phased Array type L-band Synthetic Aperture Radar) images provided by the ALOS satellite from the Japan Aerospace Exploration Agency (JAXA) over the Ecuadorian Andes. A major

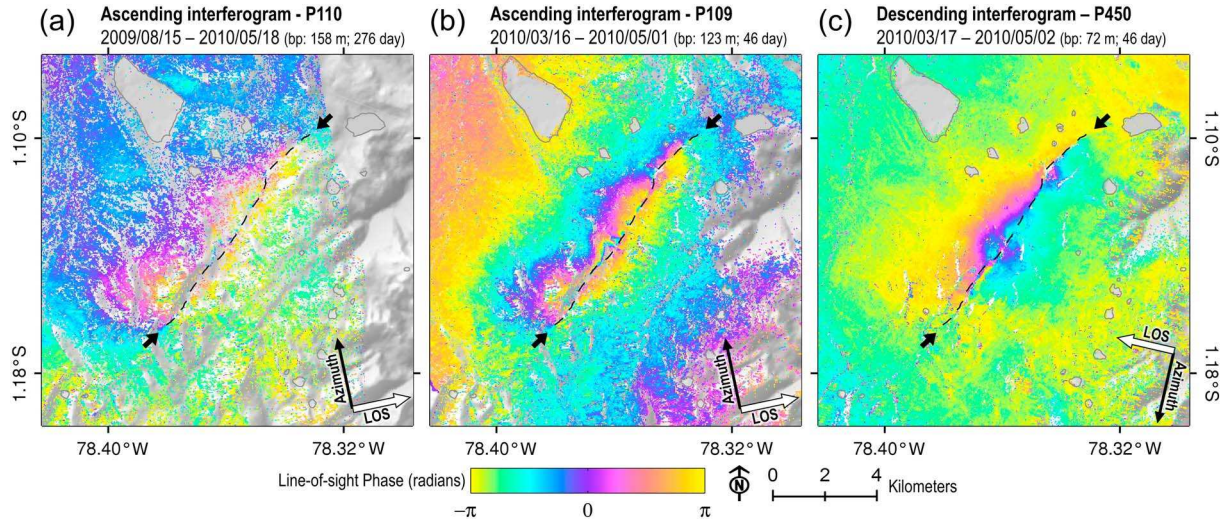

Figure 2. Wrapped interferograms with different look directions, showing surface displacement detected in the Pisayambo region. The PALSAR data were acquired (a) on 15 August 2009 and 18 May 2010 from ascending path 110; (b) on 16 March 2010 and 1 May 2010 from ascending path 109; (c) on 17 March 2009 and 2 May 2010 from descending path 450. The black dashed line represents the surface rupture as mapped using the three interferograms. The black arrows show the flight direction of the satellite, while the white arrows show line-of-sight (LOS) of the radar.

characteristic of the PALSAR sensor is that it operates in L-band, with a wavelength (λ=23.6 cm) 5 times longer than the C-band used by ERS, Envisat, or Sentinel-1. It has been shown in many regions that ALOS L-band interferograms suffer less from temporal decorrelation in vegetated areas (Champenois et al., 2012) than the C-band ones, because the longer wavelength penetrates deeper through the vegetation (Meng & Sandwell, 2010; Sandwell et al., 2008). For this reason, the PALSAR option is well suited for Ecuador, especially for the Eastern Cordillera which bounds the plains of the Amazon Basin.

A conventional Differential SAR Interferometry (DInSAR) analysis over the Eastern Cordillera of the Ecuadorian Andes is performed with ALOS images between 2007 and 2011 along the ascending paths 110 and 109 and the descending path 450 (Figure 1). All interferograms are processed with the ROI_PAC processing chain from JPL/Caltech (Rosen et al., 2004), and topographic phase component is removed with a 30 m digital elevation model (DEM) from the Instituto Geofisico in Quito (IG-EPN). Interferograms are unwrapped using the statistical-cost, network-flow phase-unwrapping algorithm (SNAPHU) (Chen & Zebker, 2001), a ROI_PAC usual unwrapper.

Based on this PALSAR interferogram data set, a substantial phase signal of surface displacement is detected in early 2010, south to the Laguna Pisayambo, between the Pisayambo fault and the Pucara fault (Figure 1b). In order to analyze these InSAR evidences of surface displacement, we select three interferograms showing surface displacement, in both ascending and descending paths (Figure 2 and Figure S1 in the supporting information), complemented by two interferograms in ascending path covering periods before and after surface displacement (Figure S2). Additionally, we process one ascending interferogram with Envisat C-band data showing surface displacement; however, radar decorrelation due to vegetation does not allow us to exploit this InSAR information.

All selected interferograms in this study show a high interferometric coherence for this area of the Ecuadorian Andes, due to optimal L-band SAR acquisition parameters with a time span between images ranging from 46 to 276 days and perpendicular baselines lower than 200 m. Additionally, these interferograms are not affected by significant atmospheric effects. The surface displacement detected in the interferograms looks similar to a tectonic phase signal such as the coseismic deformation observed after the 2014 M_w6.0 South Napa Valley earthquake in California (Barnhart et al., 2015). Moreover, a clear phase discontinuity can be followed over ≈9 km (Figures 2 and S1), indicating that a rupture reached the surface. Thanks to the high quality of the interferograms, an accurate map of the inferred surface rupture is extracted with a precision of 30–100 m. The surface rupture follows a linear trend with a general direction SW-NE, approximately N035°E. Temporally, the InSAR observations used in this study (Figures 2, S1, and S2) allow us to reduce to 16 days the time interval during which the surface displacement occurs, between 17 March 2010 and 2 April 2010.

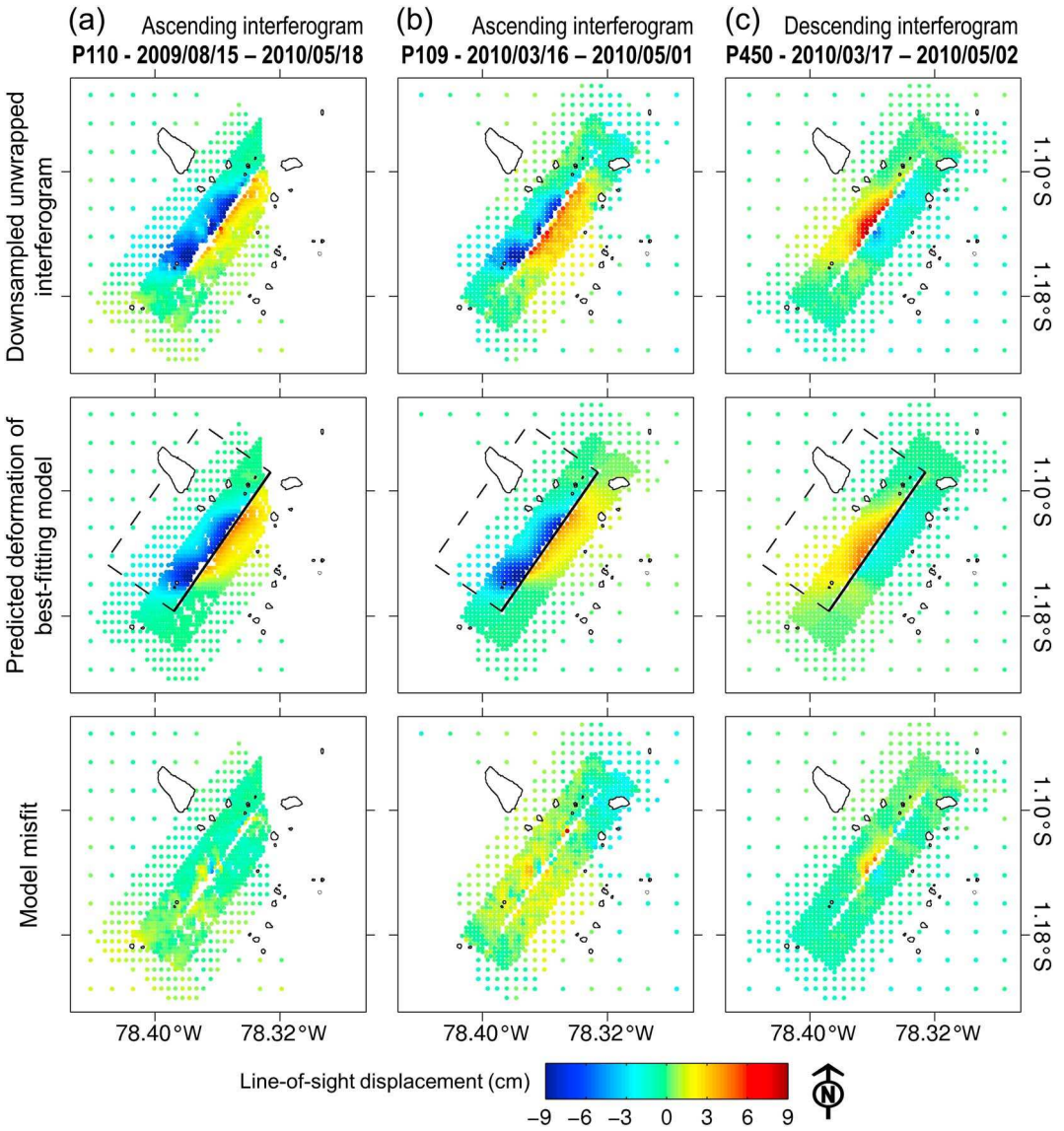

Figure 3. (top row) Downsampled interferograms of the Pisayambo region (top row),(middle row) synthetics for the best fitting single-fault model, and (bottom row) residuals between data and model. Black box represents the surface projection of the inverted fault geometry. (a) Ascending interferogram path 110. (b) Ascending interferogram path 109. (c) Descending interferogram path 450.

2.2. Slip Inversion

The quality of this InSAR data set, including multiple look directions (ascending and descending tracks), makes possible an inversion of the surface displacements following the general methodology of Barnhart and Lohman (2010) and Barnhart et al. (2014). The geodetic inversion is done using InSAR observations alone (no GPS installed in the area) in order to retrieve the strike, dip, rake, and slip distribution.

First, each unwrapped interferogram is optimally downsampled to a computationally feasible number of observations, less than 14,000, using three different grid resolutions (1,500 m, 500 m, and 250 m) (Figure 3). In order to obtain the precise fault geometry, we performed a basic analysis of several direct models of a single-fault patch in a homogeneous elastic half-space (Okada, 1992) with homogeneous slip and various rake and dip values. All best fitting models are obtained for a strike value of N215°E, corresponding to a fault plane dipping to the west. The slip surface is modeled in this case by a 12 km side square.

Fixing this strike value, we next invert the InSAR data to obtain a distributed slip model using an iterative method in which the N215°E fault plane is discretized with triangles whose size is controlled by the model

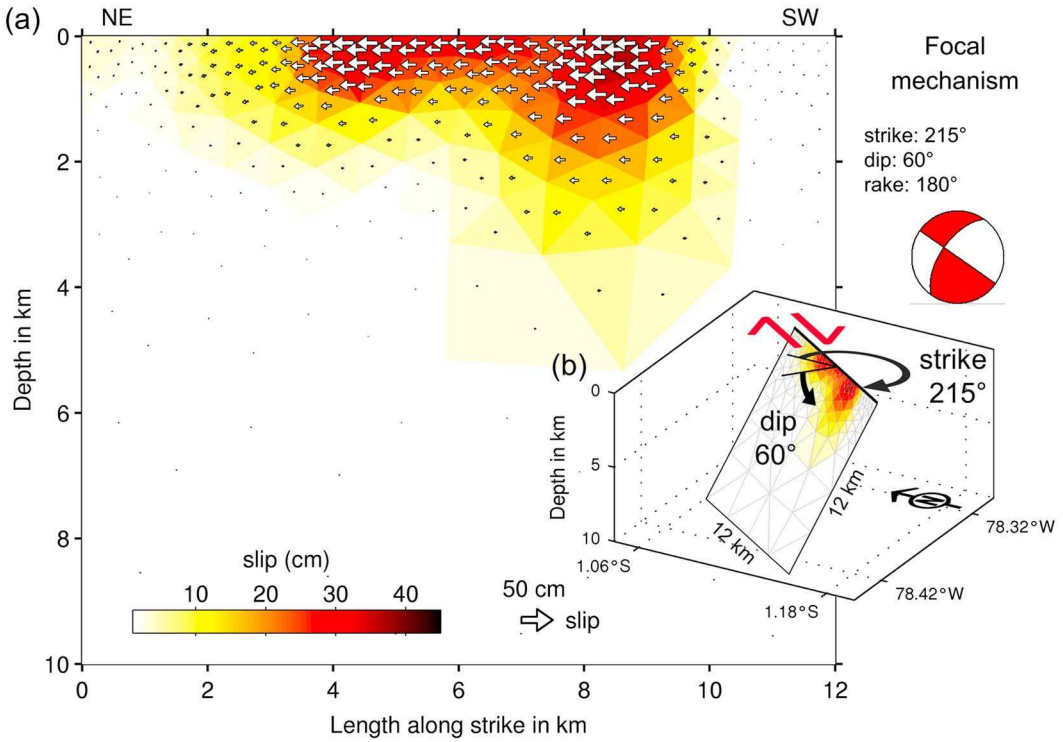

Figure 4. Slip distribution inferred from the inversion of the interferograms. (a) Slip distribution on the fault. The arrows show slip directions of the western side of the fault. (b) Perspective view of the slip distribution. Arrows indicate the dextral displacement of the fault. Dip and strike angles of fault model geometry used for the best fitting model are indicated in decimal degrees. The corresponding focal mechanism and earthquake parameters are shown in the upper right corner.

resolution (Barnhart & Lohman, 2010). The inversion of the surface displacements is tested with dip angle values ranging from 30° to 80°. For each of these inversion tests, we fix strike, fault width, and fault length but allow for a freely variable rake; we use a Laplacian smoothing matrix and choose the optimal smoothing value according to a L-curve criterion (Segall & Harris, 1987). Finally, we choose the best fitting model that minimizes the normalized root-mean-square error to the InSAR observations (Figures 4 and S3). The result of our preferred fault geometry and slip distribution inversion is obtained with a dip angle of 60° to the NW (Table S1). Regarding the rake angle values resulting from the inversion, they are homogenous and all range between 175° and 185°. They clearly indicate that the slip along the fault plane is almost exclusively right-lateral strike slip. This finding remains true whatever the dip angle used in the inversion process.

Predictions from our slip distribution model, using elastic parameters for a homogeneous crust, match well the line-of-sight surface displacement (Figures 3 and S1), with root-mean-square misfits between predicted and observed displacement of 0.74 cm, 1.18 cm, and 0.75 cm, respectively, for the three PALSAR interferograms (Figure 3). The residuals between InSAR observations and predicted displacements are larger close to the surface rupture. This can be explained by our choice of a simplified fault geometry in the slip inversion. In reality, the fault trace exhibits small variations in strike that were not accounted for in the modeling. In addition, descending InSAR observations are less well fit by our best fitting model than ascending InSAR observations (Figure 3), especially close to the central part of the surface rupture, with maximum line-of-sight residuals reaching 4–5 cm.

The slip distribution derived from our best fitting model shows that slip occurs at depths shallower than 6 km (Figure 4). The maximum slip value is 45 cm and localized close to the surface. Along strike, the slip distribution reveals two separated areas of slip with similar amplitude, one to the northeast with shallow slip between 0 and 2 km depth, and the other to the southwest with deeper slip between 0 and 6 km depth. If adopting a standard shear modulus value of 30 GPa, the equivalent earthquake moment magnitude associated with the inverted fault displacement is 5.44. The inferred focal mechanism is slightly different (Figure 4) from the one determined by GCMT (Figures 1 and 9). Strike and rake angles are similar, but the dip angles differ by about

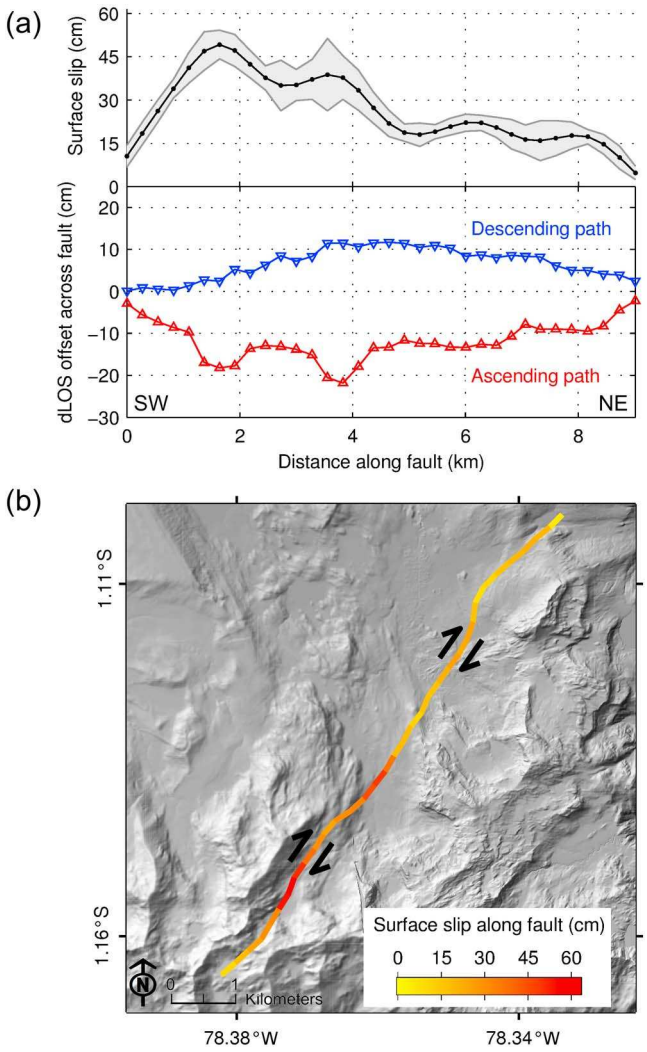

Figure 5. Estimated strike-slip movements along the fault surface inferred from 2-D analysis of interferograms. (a) Calculated values of strike-slip faulting at the ground surface (black line) as derived from the line-of-sight displacement (dLOS) offsets across the fault in both ascending path (red line) and descending path (blue line). (b) Map of strike-slip faulting at the surface superimposed on a 4 m digital elevation model.

14° (60° for our fault slip inversion compared to 74° for GCMT). Such non-vertical dip angles for strike-slip earthquakes appear to be more common than previously thought, as recently illustrated for the well-imaged 2016 Kumamoto earthquake (dip angle value of 65°, (Himematsu & Furuya, 2016)) or the large strike-slip earthquakes occurring in 2003 and 2013 along the Scotia-Antarctic plate boundary (Vallée & Satriano, 2014).

In addition to the above slip inversion relative to the deformations observed between 17 March 2010 and 2 April 2010, we also conduct pre-seismic and postseismic analyses using interferograms along the ascending path 110 (examples in Figure S2). These interferograms are relatively flat with no phase signal of surface displacement, suggesting that no surface displacements occurred before and after the March 2010 event.

2.3. Surface Rupture Displacement Estimation

In order to precisely measure the spatial variation of surface displacement along the fault trace, we use a series of 34 profiles, every 260 m, perpendicular to the main direction of the rupture. According to the source parameters derived from the slip inversion, we consider that vertical displacements are negligible across the fault, since the slip motion is fully right lateral. By using two interferograms (Figures 2b and 2c), with different line-of-sight directions, we are therefore able to estimate the horizontal displacement components for each profile across the rupture.

To do so, we first estimate the line-of-sight displacement offset (dLOS) across the fault surface rupture for both ascending (blue line on Figure 5a) and descending interferograms (red line on Figure 5a). We propagate the uncertainty by summing the two root-mean-square values of line-of-sight displacements estimated on the northwest and the southeast sides of the surface rupture. Second, the estimates of dLOS from the two different look directions are decomposed into 2-D InSAR data consisting of displacements in the north/south and west/east components. Finally, we use this 2-D displacement data set to evaluate strike-slip surface faulting all along the LPF (black line on Figure 5a).

The surface strike-slip faulting values range from 0 to 50 cm with a mean uncertainty of about 8 cm. The northern flat section of the LPF presents moderate displacements with a maximum surface slip of about 23 cm while the southern mountainous section of the LPF presents the highest surface displacement values (black line in Figure 5a and colored line on Figure 5b).

3. Geological Investigations

In this area where the Mio-Pliocene Pisayambo Formation is in contact with the basement, one can recognize that the local landscape has been shaped by active ice masses, which left curved erosional escarpments in the highest areas ("Glacial scars" in Figure 6), basal erosion grooves on polished bedrock ("Glacial grooves" in Figure 6), as well as moraines (see the "Moraine contour" that depicts the extension of the most recent tills of the area). These moraines are probably, considering their very high elevation (3,800 – 4,000 m), associated with the Younger Dryas cold event that has been recognized and dated along the Chimborazo slopes (Clapperton, 1990; Samaniego et al., 2012).

During a 1 week field survey in October 2014, the occurrence of fresh surface faulting was clearly identified. A total of 40 waypoints (wpt) were recorded along a 5 km long portion of the fault identified by geodetic analysis (Figure 6b). Figure 7 provides examples of fresh surface faulting which were systematically mapped along a cumulative fault (the so-called Laguna Pisayambo Fault) evidenced by offsets of various morphological features and deposits associated with the glacial age. We have documented scarps, pressure ridges, offset

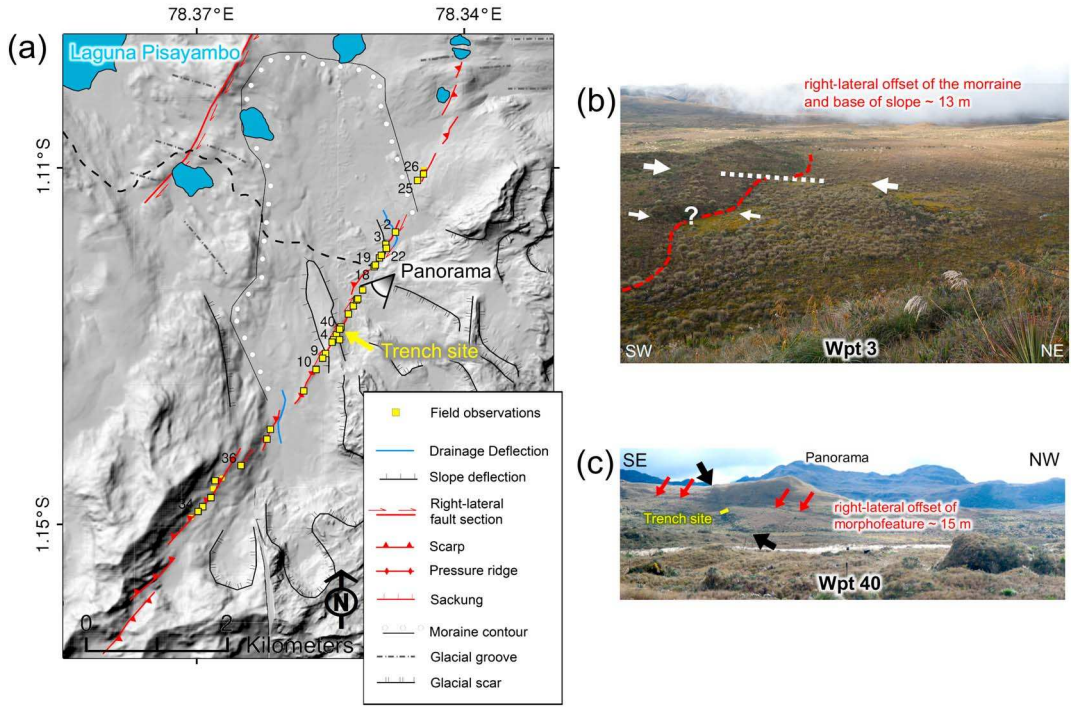

Figure 6. The Laguna Pisayambo Fault. (a) The 4 m DEM topography (IG-EPN data set) of the study area, with the observation points, (yellow squares) where we could get cumulative and last slip event displacement measurements (yellow dots); the map includes the main glacial and postglacial morphological features, as well as the major morphotectonic lines interpreted from DEM and SPOT6 images; (b) one fault strand dextrally displaces the moraine by 13 m, where clear fresh fractures were observed (one possible other cumulative fault section could not be confirmed by recent rupture clues); [not easy to follow] farther north (not on picture), the current channel is deflected by the same amount (wpt 3);(c) the cumulative fault scarp (black arrows) displaces a morphological marker (red arrows) by about 15 m; the handmade trench was dug there (wpt 40).

slopes or deflected channels, and displaced moraines, which depict the dominant right-lateral and secondary vertical components (western side up).

3.1. Evidences of the LPF Long-Term Activity

In the northernmost investigated section, the fault trace is shown by a low-relief counterscarp with a cumulative dextral offset of about 10 m (wpt 26 in Figure 6b). In the northern central section of the surface rupture, close to the path (wpt 2 to 3, 18 to 22 in Figure 6b), the moraines are dextrally displaced by about 12–15 m, with a small vertical component (1 m) (wpt 3 in Figure 6b); the current drainage network is also laterally deflected by the same amount (wpt 2). Along the hillslopes of the central section (between wpt 40 and 10; Figure 6), several morphological features are dextrally displaced by about 15 m as well. The panoramic view (Figure 6c) depicts the fault scarp offsetting a slope gradient, that could correspond to a lateral moraine scarplet (because of its connection to glacial scars; wpt 40). To the south (wpt 34 in Figure 6b), the fault trace is clear, with eastward asymmetrical pressure ridge (wpt 10) or scarps, but the geomorphological context prevents the estimation of the cumulative dextral component: the fault scarp directly bounds the flat marsh with the dissected hillslopes and no piercing line can be identified to estimate the horizontal slip. In this area (wpt 36 in Figure 6b), we found significant secondary gravitational movements (sackung and landslides). In a short and shallow hand-excavated trench (wpt 40 in Figure 6b; Figure S4), we unearthed the young sediments that lay beneath the ground surface, with black organic soils (andisols) overlying reddish, massive, and poorly sorted conglomerates. In the geomorphologic context, the surface soils (thickness larger than 2 m) are typical of the current environment (Holocene paramo), whereas the conglomerates should correspond to Pleistocene moraines. The trench evidences the vertical separation of the moraine and the fault zone between the uplifted (western) and downthrown (eastern) walls, as well as the network of fresh and open fractures. At the base of the section, two levels of moraine-like pebbles are intercalated within the black andisol (yellow dots in Figure 6c). These two levels could correspond to classical colluvial wedges associated with the

Figure 7. Field observations of the 2010 surface rupture evidences (a) in the southern part of the 2010 surface rupture, a large and wide open crack is observed 10 m west of the cumulative scarp (black arrows); (b) in the central section, the track is cut by the rupture; there we measured a right-lateral displacement of 20 cm and a vertical displacement of 10 cm.

degradation of the nearby moraines, uncovered during morphogenic faulting events (i.e., two paleoearthquakes) but the paucity of stratification precludes any definitive conclusion on fault slip history.

3.2. The 2010 Surface Displacement Along the LPF

The LPF fault is without a doubt an active fault able to generate surface displacement. This is suggested by its morphological imprint and is directly evidenced by the fresh surface faulting detected along a 5 km long portion of the fault, where geodetic analyses also revealed fault displacements. Due to limited accessibility, we unfortunately could not reach the rest of the fault line. In particular, the locations with major displacements identified by InSAR analysis (d=50 cm) are not documented with field measurements.

The evidence for displacement is mainly open cracks, fractures with offsets, and N030°-to-N050°E pop-up features. Several en echelon fissures are also documented; their N070°-to-N080°E mean strike is consistent with deep-seated N040°E dextral strike-slip faulting. Despite a 4.5 year long postslip time span, we propose that these fresh features are associated with the 2010 slip event. These could have been preserved because of the stiffness of the andisol and the absorption capacity of the vegetation, precluding the runoff, the erosion, and resedimentation. The only imprint of time is the lichen coating the walls of the fissures.

Most of the observations validate the purely dextral component of displacement with the opening of small-scale pull-apart depressions (e.g., wpt 04, 09, 25, and 34 in Figure 6b), with measured values ranging between 15 and 30 cm in agreement with the geodetical analysis results. In some places, small vertical offsets were observed (wpt 19, and 25 in Figure 6b), occasionally of the same order as horizontal ones (e.g., wpt 10 in Figure 6b). In the southern section, the significant vertical component could have been increased by local gravitational movements, as observed apart from the surface rupture. With the available field evidences, we do not have the definitive proof that they are purely coseismic in origin, or partly/totally due to an aseismic/creeping event occurring during the 16 day time window of the InSAR data. However, we note that the

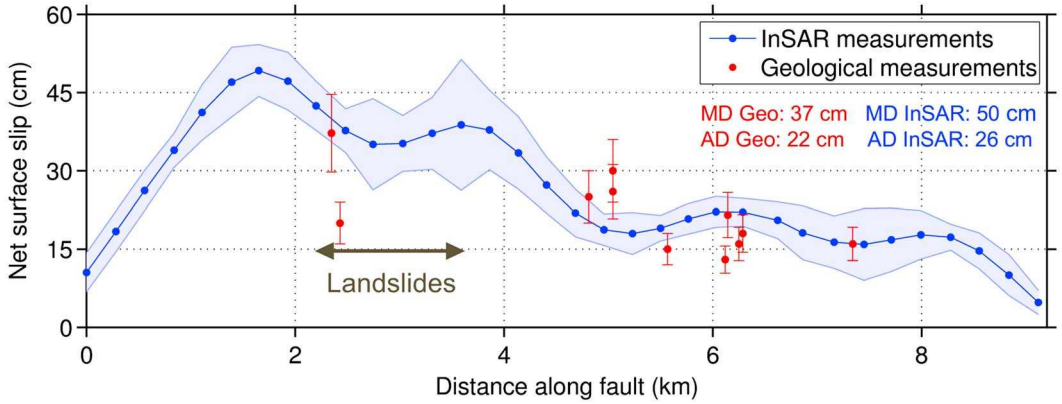

Figure 8. Comparison of estimated strike-slip faulting along surface fault (SW-NE profile) as inferred from InSAR measurements (blue dots) and observed from geological field measurements (red crosses). The double arrow indicates landslide areas observed in the field. MD and AD represent estimations of Maximum Displacement and Average Displacement, respectively.

interferograms before and above all after the slip event (March 2010) do not show any activity along the fault line (Figure S2).

We stress that all along the surface fault trace, we could not find any proof of previous historical surface rupture. In 1949, the region was, however, hit by a severe earthquake (the so-called Pelileo earthquake) whose magnitude has been estimated to *M*6.3–6.6 (Beauval et al., 2010). The instrumental epicenter location is close to the Laguna Pisayambo Fault, but the uncertainties are expected to be large for such an old event. In contrast, the macroseismic epicenter, 20 km to the southwest of the fault, is probably more accurately located because of the numerous data available in the epicentral area (Beauval et al., 2010). For these reasons, it seems unlikely that the LPF has been repeatedly activated by the 1949 Pelileo and 2010 Pisayambo earthquakes.

In quantitative terms, we conclude that the 2010 slip event occurred along a 9 km long surface fault line, with maximum displacement (MD) of 37 cm (field measurement) to 50 cm (InSAR data) and average displacement (AD) of 22 cm (field measurement, but non exhaustive) to 26 cm (InSAR data) (Figure 8).

4. Seismological Analysis

Based on the previous sections favoring a coseismic rupture, we were expecting that a significant earthquake (M_w~5.5) occurred during the time window of the interferograms showing surface displacements (17 March to 2 April 2010) and close (<10 km) to the mapped surface displacement. A first-order analysis of the Worldwide and Ecuadorian seismic catalog surprisingly does not reveal such an event. However, if considering a wider area, the cumulated seismic moment clearly increases in the target period (Figure 9), mostly due to the occurrence of a *M*5 earthquake (26 March 2010), identified and located in the IG-EPN local hypocenter catalog, the ISC hypocenter catalog, and Global CMT catalog of moment tensors.

The location differences (up to 30 km) between the different institutes reflect the usual uncertainty in locating earthquakes in the absence of a dense local network. It also indicates that this earthquake can be realistically located on the fault imaged by InSAR analysis. The hypothesis that the earthquake is responsible for the slip episode is even more plausible as (1) it is the strongest seismic event in the area according to IG-EPN local catalog and (2) the Global CMT provides a focal mechanism consistent with the conclusions of our geodetic and geological study (Figure 9).

However, the 4.9–5 magnitude found by all the institutes (IG-EPN, ISC, and Global CMT) is far below the 5.44 value estimated by InSAR analysis using a standard rigidity for the crust (30 GPa). This magnitude difference corresponds to a seismic moment ratio of about 5. A first hypothesis able to reconcile these two different values would be that the observed surface slip includes a large part of afterslip (i.e., aseismic slip on the ruptured fault) following the *M*5 earthquake. This phenomenon has been described after moderate strike-slip events such as the 1987 Superstition Hills (Bilham, 1989) or the 2014 Napa (Lienkaemper et al., 2016) events in California. However, if using this unique explanation, an unusual amount of postseismic slip, on the order of 400–500% of the coseismic one and released in only 6 days, has to be invoked. Furthermore, after being

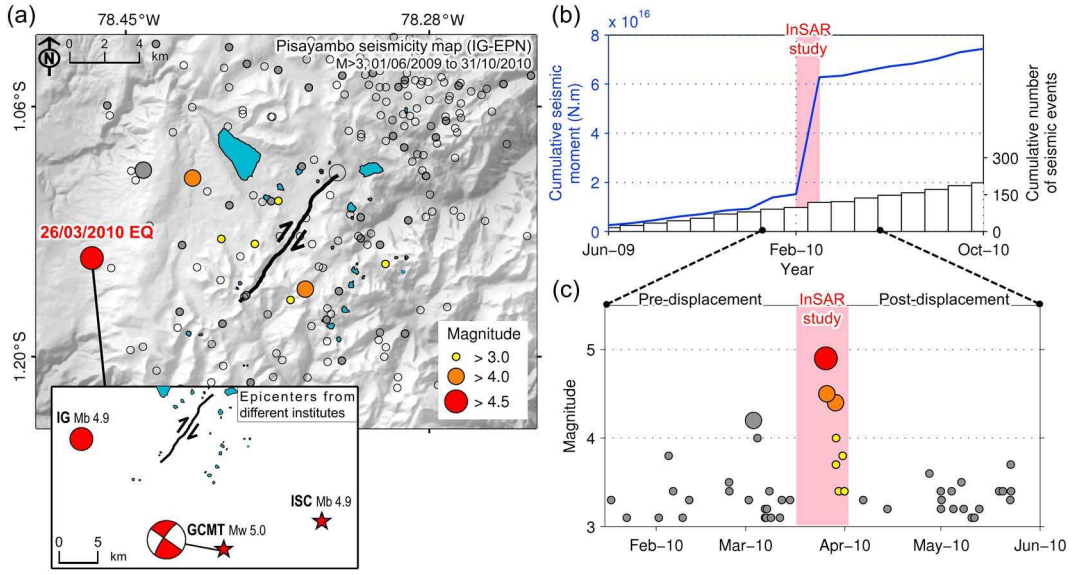

Figure 9. Recorded seismicity in the Pisayambo area between June 2009 and October 2010 from IG-EPN (apps.igepn.edu.ec/cnd). (a) Seismicity map surrounding the study area of all earthquakes with magnitude >3. The black line represents the surface rupture derived from this InSAR study. Colored points indicate earthquakes that occurred during the observed deformation period. The left bottom map presents the different locations for the main *M*5.0 earthquake that occurred on 26 March 2010. The computed Global CMT focal mechanism parameters for this event are as follows: Strike 215°, Dip 74°, and Rake −180°. (b) Cumulative seismic moment (blue line) and cumulative number of seismic events (histogram). (c) Magnitudes of earthquakes recorded 60 days before and after the InSAR time window of the detected surface displacement event (red area).

very active in the days following the earthquake, this postseismic phase should have abruptly stopped, to agree with the absence of detectable deformation signal in the later pairs of SAR images. This behavior would therefore be different from the exponential decay usually observed for postseismic processes. Other explanations should therefore be considered. We focus our attention on the rigidity μ, knowing that geodetic analyses are essentially not sensitive to this parameter, while seismological moment magnitudes are. If rigidity in the source area is 5 times lower than the standard one in the crust, the seismic moment derived from InSAR would be M_w5, on the same order than the seismic one. As InSAR analysis unequivocally shows that the slip episode is very shallow (<3 km), at depths where Earth materials can be unconsolidated, this hypothesis of low rigidity is realistic.

In order to test this idea quantitatively, we explore how seismograms recorded on local and regional broadband stations of the Ecuadorian network can be modeled in the case of a very shallow hypocenter. We conduct an inversion based on the discrete wave number method (Bouchon, 1981), where we constrain the focal depth to be shallow (<2.5 km) and allow for a low-rigidity upper layer. We search for focal mechanisms with a geometry close to that obtained in the InSAR analysis. The best model, shown in Figure 10, has a hypocentral depth of 1.5 km, embedded in a layer with a low rigidity of 6 GPa (shear velocity of 1.9 km/s and density of 1,700 kg/m^3). In the 0.03 Hz–0.05 Hz frequency range, in which the displacement data are inverted, the agreement is good for all the components (see a subset of the stations in Figure 9 and all the waveforms in Figure S5). The strike-slip focal mechanism is in agreement with the InSAR analysis, including the northwestward dipping character of the northeast-southwest striking plane. Interestingly, the moment magnitude found by the inversion remains in the range 4.9–5.

To investigate further the effects of local elastic structure and hypocentral depth on the determination of the seismic moment, we revisited the event using the global data set and the algorithms used in the Global CMT analysis (Ekström et al., 2012). In the routine application of the software, the elastic structure at the seismic source assumed in the analysis is that of the average 1-D Earth. In the original analysis of the 26 March 2010 earthquake, this was the structure of PREM (Dziewonski & Anderson, 1985). However, the CMT analysis tool allows for adjustments to the elastic structure at the source, and we investigated the sensitivity of the CMT source parameters to both elastic structure and the source depth. The result of these experiments was that the moment-tensor results were remarkably robust even when the source was placed at a depth of 1.5 km, and

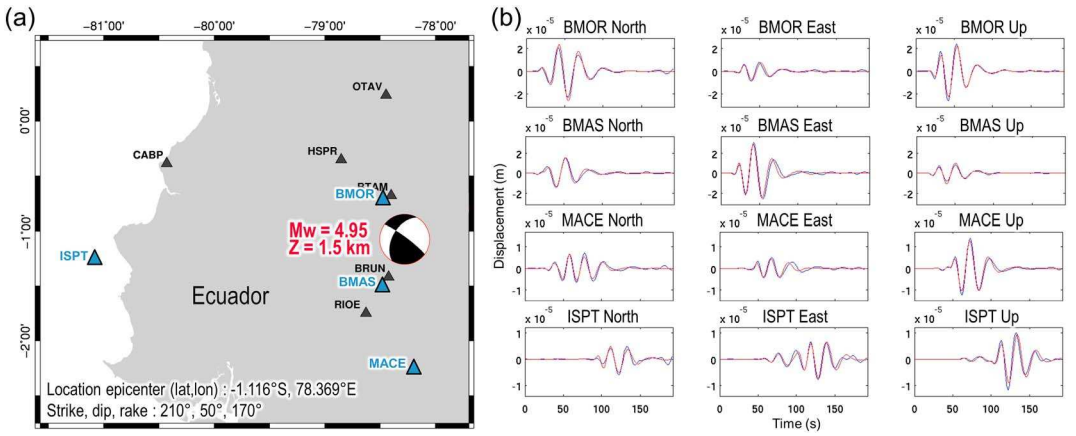

Figure 10. Source parameters of the 26 March 2010 earthquake retrieved by inversion of the local and regional broadband stations. (a) Triangles show broadband stations (IG-EPN, JICA, and ADN networks, complemented with the OTAV station of the Global Seismographic Network) used in the inversion. Displacement waveforms at these stations are modeled in the 0.03–0.05 Hz frequency range. Optimal values for the focal mechanism, moment magnitude, depth, and epicenter location are shown on the map. (b) Comparison of data and synthetics, shown for a subset of the stations corresponding to the blue triangles in the map (Figure 10a). Data are shown in blue and synthetics in red, for the three components of the displacement at each station. Comparison of data and synthetics at all stations can be seen in Figure S5 in the supporting information.

the elastic parameters for the top 3 km layer were chosen to agree with those used in the geodetic modeling. Specifically, the seismic moment determined using the Global CMT algorithm employing an appropriate local elastic structure at the source, and a hypocentral depth of 1.5 km, was smaller by only ~30% than the value obtained in the standard CMT analysis.

As a final argument favoring the hypothesis of a shallow earthquake in a low-rigidity medium, the source duration found by the local and regional broadband inversion is long (5 s) for an earthquake of this magnitude. This is expected, as rupture velocity, which is controlled by the shear velocity, should be slow in a low-rigidity medium. The 26 March 2010 earthquake can therefore be interpreted as a continental analog of the slow earthquakes observed in the very shallow part of the subduction interface (e.g., the M_w=7.6 2 September 1992 Nicaragua earthquake (Kanamori & Kikuchi, 1993) or the M_w=7.9 25 October 2010 Mentawai, Indonesia, earthquake (Newman et al., 2011)). These earthquakes also occur in inconsolidated media with low rigidity. As a consequence, they propagate at slow rupture velocities and generate large seafloor displacements with respect to their magnitudes (at the origin of abnormally high tsunami waves).

Seismological analysis therefore supports the interpretation that the 26 March 2010 earthquake is responsible for a large part, or even all, of the slip episode detected by the InSAR analysis. The initial discrepancy in terms of magnitude disappears if we take into account a low-rigidity layer: this is realistic for such a shallow event, and leads to the same moment magnitude (4.9–5) for the InSAR and seismological analyses, in both cases with a very good fit to the data.

5. Discussion and Conclusions

The combination of InSAR, geological, and seismological observations illuminates the anomalous length-slip-magnitude relations of the *M*5 2010 earthquake. According to the classical empirical relationship from Wells and Coppersmith (1994), a maximum displacement MD=50±8 cm or an average displacement AD=25 cm could be associated with a *M*6.5 event, and a surface rupture length SRL=9 km to a *M*6.2 one. Similarly, the moment magnitude scale of Hanks and Kanamori (1979) gives a *M*6.3 event for the same AD-SRL and assuming a classical shear modulus value of μ=30 GPa.

Low-magnitude earthquake and high surface faulting values can be reconciled if considering either that (1) the *M*5 earthquake was followed by significant afterslip in a rigid crust and/or (2) that all the observed displacement occurred co-seismically at a very shallow depth in a low rigidity crust (consistently with our seismological analysis). After well-known crustal earthquakes, several authors have shown that afterslip has been accommodated over relatively long time periods (weeks or months), whatever the magnitude (Bilham, 1989;

Lienkaemper & McFarland, 2017; Lienkaemper et al., 2016; Omata et al., 2017; Shirahama et al., 2016). After crustal strike-slip earthquakes in California, 50–80% and 65% of the total slip had been measured in 6 days on creeping parts of the surface rupture, respectively, after the 1987 *M*6+ Superstition Hills earthquake doublet (McGill et al. 1989) and the 2014 *M*6 Napa earthquake (Lienkaemper et al., 2016). If these rates are applied to the Pisayambo case and if we only consider hypothesis (1), this means that 5 to 15 cm (1/3 of 15 to 45 cm) of surface faulting should have been accommodated after the InSAR time frame (ending on 2 April 2010). However, when looking carefully at the postquake interferograms (Figure S2), this hypothesis appears unlikely as no continuing geodetic deformation was detected.

If afterslip is the only reason explaining the observed differences between geometric and seismic moment, this also implies a very high aseismic/seismic ratio. The aseismic processes would multiply, in only 6 days, the coseismic slip by a factor of 4–5. Examples of such an energetic postseismic phase do not appear to have been documented. Our seismogeodetical analysis, favoring the hypothesis of a low-rigidity medium, does not rule out the existence of complementary postseismic processes, which are frequently observed after earthquakes. The advantage of the low-rigidity faulting hypothesis is to offer an explanation that does not require rapid aseismic deformation that greatly exceeds the coseismic slip in the week following the earthquake. We finally emphasize that such seismic processes in inconsolidated media, even if poorly documented in continental contexts, are known to occur in the very shallow part of the subduction interface. As inferred for the Pisayambo earthquake, the latter events (referred as "slow earthquakes" or "tsunami earthquakes") generate abnormally large ground displacement amplitudes.

The Pisayambo rupture is also characterized by a high aspect ratio (4:1) for such a small event. According to the linear relationship between this ratio and the surface length presented by Wesnosky (2008) [Aspect ratio (SRL/W) = 0.088 × SRL], the 4:1 value obtained here is consistent with a SRL 45 km event (i.e., a magnitude around 7). This moderate and shallow earthquake therefore poses the question of applicability of classical empirical relationships providing regressions between magnitude and fault parameters without accounting for focal depth or crustal rigidity (Wells & Coppersmith, 1994). We also point out that the empirical relationships, extensively used by geologists in seismic hazard analyses, should be compared with results on recent events documented with accurate data of surface displacements (InSAR, LiDAR, etc), with known focal depth and realistic rheology of the crust and estimation of afterslip contribution.

This study of a moderate earthquake rupture reaching the surface highlights the value of applying InSAR methods for the characterization of low-magnitude events. Indeed, as illustrated by the 2010 Pisayambo earthquake, InSAR analysis can provide meaningful information about earthquake location, fault geometry, earthquake source mechanisms, and magnitude, as is currently typically obtained only for larger (M>6) events. All this information is very valuable, as it makes possible the extension of scaling studies of shallow earthquakes—particularly relevant for seismic hazard—toward smaller magnitudes. It can also be used, in complement to the surface displacements data sets, to assess better the variability of these widely used scaling laws and to compute statistics on the probability of future surface displacements (Petersen et al., 2011).

Acknowledgments
This project was partly supported by the Japan Aerospace Exploration Agency (JAXA) which delivered ALOS-1 PALSAR data in the scope of PI 1289002 project. Part of this project was supported by French Centre National d'Etudes Spatiales (CNES) and French Institut de Recherche pour le Développement (IRD). The regional seismological analysis uses seismic stations from the IG-EPN network from IG-EPN (apps.igepn.edu.ec), built in cooperation with French ANR project "Andes du Nord" (contract ANR-07-BLAN-0143-01) and JICA (Japan International Cooperation Agency). Data from the global FDSN network of seismic stations (www.fdsn.org/networks), including from station OTAV in Ecuador, were also used in this study. Additional Earthquake source parameters were downloaded from GCMT (http://www.globalcmt.org/) and ISC (http://www.isc.ac.uk/). The authors are grateful to W. D. Barnhart for developing and offering access to the "FaultResampler" freeware (http://myweb.uiowa.edu/wbarnhart/programs.html) and to H. Lyon-Caen for discussion. We thank R. Bilham, P. Tregoning, and two anonymous reviewers for insightful comments.

References

Alvarado, A. (2012). Néotectonique et cinématique de la déformation continentale en Equateur (Ph.D. thesis), (Alvarado cevallos) Thèse de doctorat Sciences de l'univers Grenoble. 2012GRENU026.

Baize, S., Audin, L., Winter, T., Alvarado, A., Pilatasig Moreno, L., Taipe, M., … Yepes, H. (2015). Paleoseismology and tectonic geomorphology of the Pallatanga fault (Central Ecuador), a major structure of the South-American crust. *Geomorphology*, *237*, 14–28.

Barnhart, W. D., & Lohman, R. B. (2010). Automated fault model discretization for inversions for coseismic slip distributions. *Journal of Geophysical Research*, *115*, B10419. https://doi.org/10.1029/2010JB007545

Barnhart, W. D., Benz, H. M., Hayes, G. P., Rubinstein, J. L., & Bergman, E. (2014). Seismological and geodetic constraints on the 2011 M_W5.3 Trinidad, Colorado earthquake and induced deformation in the Raton basin. *Journal of Geophysical Research: Solid Earth*, *119*, 7923–7933. https://doi.org/10.1002/2014JB011227

Barnhart, W. D., Murray, J. R., Yun, S., Svarc, J. L., Samsonov, S. V., Fielding, E. J., … Milillo, P. (2015). Geodetic constraints on the 2014 *M* 6.0 South Napa earthquake. *Seismological Research Letters*, *86*(2A), 335–343.

Beauval, C., Yepes, H., Bakun, W. H., Egred, J., Alvarado, A., & Singaucho, J. C. (2010). Locations and magnitudes of historical earthquakes in the Sierra of Ecuador (1587–1996). *Geophysical Journal International*, *181*, 1613–1633. https://doi.org/10.1111/j.1365-246X.2010.04569.x

Bilham, R. (1989). Surface slip subsequent to the 24 November 1987 Superstition Hills, earthquake, California, monitored by digital creepmeters. *Bulletin of the Seismological Society of America*, *79*(2), 425–450.

Bouchon, M. (1981). A simple method to calculate Green functions for elastic layered media. *Bulletin of the Seismological Society of America*, *71*(2), 959–971.

Champenois, J., Fruneau, B., Pathier, E., Deffontaines, B., Lin, K. C., & Hu, J. C. (2012). Monitoring of active tectonic deformations in the Longitudinal Valley (Eastern Taiwan) using persistent scatterer InSAR method with AlOS PALSAR data. *Earth and Planetary Science Letters*, *337–338*, 144–155.

Chen, C. W., & Zebker, H. A. (2001). Two-dimensional phase unwrapping with use of statistical models for cost functions in nonlinear optimization. *Journal of the Optical Society of America A*, *18*(2), 338–351.
Clapperton, C. M. (1990). Glacial and volcanic geomorphology of the Chimborazo-Carihuairazo Massif, Ecuadorian Andes. *Earth and Environmental Science Transactions of the Royal Society of Edinburgh*, *81*(02), 91–116.
Dziewonski, A. M., & Anderson, D. L. (1985). Preliminary reference Earth model. *Physics of the Earth and Planetary Interiors*, *25*(4), 297–356.
Ekström, G., Nettles, M., & Dziewonski, A. M. (2012). The global CMT project 2004–2010: Centroid-moment tensors for 13,017 earthquakes. *Physics of the Earth and Planetary Interiors*, *200-201*, 1–9.
Hanks, T. C., & Kanamori, H. (1979). A moment magnitude scale. *Journal of Geophysical Research*, *84*(B5), 2348–2350.
Himematsu, Y., & Furuya, M. (2016). Fault source model for the 2016 Kumamoto earthquake sequence based on ALOS-2/PALSAR-2 pixel-offset data: Evidence for dynamic slip partitioning. *Earth, Planets and Space*, *68*, 169.
Kanamori, H., & Kikuchi, M. (1993). The 1992 Nicaragua earthquake: A slow tsunami earthquake associated with subducted sediments. *Nature*, *361*, 714–716.
Lienkaemper, J. J., & McFarland, F. S. (2017). Long-term afterslip of the 2004 *M* 6.0 Parkfield, California, earthquake–Implications for forecasting amount and duration of afterslip on other major creeping faults. *Bulletin of the Seismological Society of America*, *107*(3), 1082–1093.
Lienkaemper, J. J., DeLong, S. B., Domrose, C. J., & Rosa, C. M. (2016). Afterslip behavior following the 2014 *M* 6.0 South Napa earthquake with implications for afterslip forecasting on other seismogenic faults. *Journal of Seismological Research Letters*, *88*(3), 609–619.
McGill, S. F., Allen, C. R., Hudnut, K. W., Johnson, D. C., Miller, W. F., & Sieh, K. E. (1989). Slip on the Superstition Hills fault and on nearby faults associated with the 24 November 1987 Elmore Ranch and Superstition Hills earthquakes, southern California. *Bulletin of the Seismological Society of America*, *79*, 362–375.
Meng, W., & Sandwell, D. T. (2010). Decorrelation of L-band and C-band interferometry over vegetated areas in California. *IEEE Transactions on Geoscience and Remote Sensing*, *48*(7), 2942–2952.
Newman, A. V., Hayes, G., Wei, Y., & Convers, J. (2011). The 25 October 2010 Mentawai tsunami earthquake, from real-time discriminants, finite-fault rupture, and tsunami excitation. *Geophysical Research Letters*, *38*, L05302. https://doi.org/10.1029/2010GL046498
Nocquet, J.-M., Villegas-Lanza, J., Chlieh, M., Mothes, P., Rolandone, F., Jarrin, P., … Bondoux, F. (2014). Motion of continental slivers and creeping subduction in the Northern Andes. *Nature Geoscience*, *7*(4), 287–291.
Okada, Y. (1992). Internal deformation due to shear and tensile faults in a half-space. *Bulletin of the Seismological Society of America*, *82*(2), 1018–1040.
Omata, M., Sango, D., Kohriya, Y., & Shibuya, N. (2017). Post-seismic deformation extracted by InSAR after the 2014 Northern Nagano Prefecture earthquake. JJpGU-AGU, S-SS12-P05.
Pennington, W. D. (1981). Subduction of the Eastern Panama basin and seismotectonics of Northwestern South America. *Journal of Geophysical Research*, *86*(B11), 10,753–10,770.
Petersen, M. D., Dawson, T. E., Chen, R., Cao, T., Wills, C. J., Schwartz, D. P., & Frankel, A. D. (2011). Fault displacement hazard for strike-slip faults. *Bulletin of the Seismological Society of America*, *101*(2), 805–825.
Rosen, P. A., Henley, S., Peltzer, G., & Simons, M. (2004). Updated repeat orbit interferometry package released. *Eos Trans. AGU*, *85*, 47.
Samaniego, P., Barba, D., Robin, C., Fornari, M., & Bernard, B. (2012). Eruptive history of Chimborazo volcano (Ecuador): A large, ice-capped and hazardous compound volcano in the Northern Andes. *Journal of Volcanology and Geothermal Research*, *221–222*, 33–51.
Sandwell, D. T., Myer, D., Mellors, R., Shimada, M., Brooks, B., & Foster, J. (2008). Accuracy and resolution of ALOS interferometry: Vector deformation maps of the father's day intrusion at Kilauea. *IEEE Transactions on Geoscience and Remote Sensing*, *46*(11), 3524–3534.
Segall, P., & Harris, R. (1987). Earthquake deformation cycle on the San Andreas fault near Parkfield, California. *Journal of Geophysical Research*, *92*(B10), 10,511–10,525.
Shirahama, Y., Yoshimi, M., Awata, Y., Maruyama, T., Azuma, T., Miyashita, Y., … Miyakawa, A. (2016). Characteristics of the surface ruptures associated with the 2016 Kumamoto earthquake sequence, central Kyushu, Japan. *Earth, Planets and Space*, *68*, 191.
Vallée, M., & Satriano, C. (2014). Ten-year recurrence time between two major earthquakes affecting the same fault segment. *Geophysical Research Letters*, *41*, 2312–2318. https://doi.org/10.1002/2014GL059465
Wells, D. L., & Coppersmith, K. J. (1994). New empirical relationships among magnitude, rupture length, rupture width, rupture area, and surface displacement. *Bulletin of the Seismological Society of America*, *84*(4), 974–1002.
Wesnosky, S. G. (2008). Displacement and geometrical characteristics of earthquake surface ruptures: Issues and implications for seismic-hazard analysis and the process of earthquake rupture. *Bulletin of the Seismological Society of America*, *98*(4), 1609–1632.
Yepes, H., Audin, A., Alvarado, A., Beauval, C., Aguilar, J., Font, Y., & Cotton, F. (2016). A new view for the geodynamics of Ecuador: Implication in seismogenic source definition and seismic hazard assessment. *Tectonics*, *35*(5), 1249–1279.

Supporting Information for "Evidences of surface rupture associated with a low magnitude (Mw5.0) shallow earthquake in the Ecuadorian Andes"

J. Champenois,[1,2], S. Baize,[1], M. Vallée,[2], H. Jomard,[1], A. Alvarado,[3], P. Espin,[3], G. Ekstrom,[4] and L. Audin,[5]

Corresponding author: J. Champenois, Department of Tectonics, Institut de Physique du Globe, 1 rue de Jussieu, Paris, France. (champenoisjohann@gmail.com)

[1]Seismic Hazard Division, Institut de Radioprotection et de Sûreté Nucléaire, Fontenay-aux-Roses, France.

[2]Institut de Physique du Globe de Paris UMR 7154, Paris, France.

[3]Instituto Geofisico, Escuela Politecnica Nacional, Quito, Ecuador.

[4]Department of Earth and Environmental Sciences, Columbia University, New York, USA.

[5]Institut des Sciences de la Terre UMR 5275, Grenoble, France.

Contents of this file

1. Captions for Figures S1 to S5

2. Caption for Dataset 1

Introduction

Supporting information contains extra figures of InSAR results, rms misfit of fault model versus fault dip, fault trench informations, all source parameters of the 2010/03/26 earthquake retrieved by inversion of the local and regional broadband stations and data of final result for slip inversion.

Figure S1. Comparison between estimated and observed line-of-sight displacement (dLOS) profiles. The upper panels show the unwrapped interferograms while the lower panels show modeled profiles in red and observed profiles in blue along the four black lines represented in the upper panels. Shaded profiles represent the corresponding topography. (a) PALSAR interferogram in ascending path 109 between 16 March 2010 and 01 May 2010. (b) PALSAR interferogram in descending path 450 between 17 March 2009 and 02 May 2010.

Figure S2. Pre- and post-displacement unwrapped interferograms with observed line-of-sight displacement (dLOS) profiles. The lower panels show observed profiles in blue along the four black lines represented in the upper panels. Shaded profiles represent the corresponding topography. (a) PALSAR interferogram in ascending path 110 between 15 August 2009 and 31 December 2009. (b) PALSAR interferogram in ascending path 110 between 02 April 2010 and 18 May 2010.

Figure S3. RMS misfit plot for various fault dip angle model. The red circle shows the best-fit dip model shown in the Figures 3 and 4.

Figure S4. North facing wall of the hand-made trench (50 cm-spacing grid) depicting the main fault zone (red dashed lines) between the Pleistocene moraine and the Holocene andisol. The 2010 related surface rupture fractures are indicated in white dashed lines). C14 datings of samples (white squares) are calibrated and given in calendar ages. Alignments of pebbles point out two colluvial wedges associated with morphogenic paleo-earthquakes (one between -2500 and -1070 cal B.C; one between -840 and -340 cal B.C), which have lifted the moraine to crop out.

Table S1. Data from slip inversion with slip value (in cm), rake angle (in degree), Lon/Lat/Depth coordinates (in UTM) for each patch.

Figure S5. Source parameters of the 2010/03/26 earthquake retrieved by inversion of the local and regional broadband stations. Triangles show broadband stations (IG-EPN, JICA and ADN networks, completed with the OTAV station of the Global Seismic Network) used in the inversion. Displacement waveforms at these stations are modeled in the 0.03-0.05Hz frequency range. Optimal values for the focal mechanism, moment magnitude, depth, and epicenter location are shown on the map. Data agreement between data in red and synthetics in blue for the three components of the displacement at each station.

Figure DS1. Slip distribution data. Height columns with respectively: slip value (cm), rake angle, and mesh coordinates (Lon/Lat/Z).

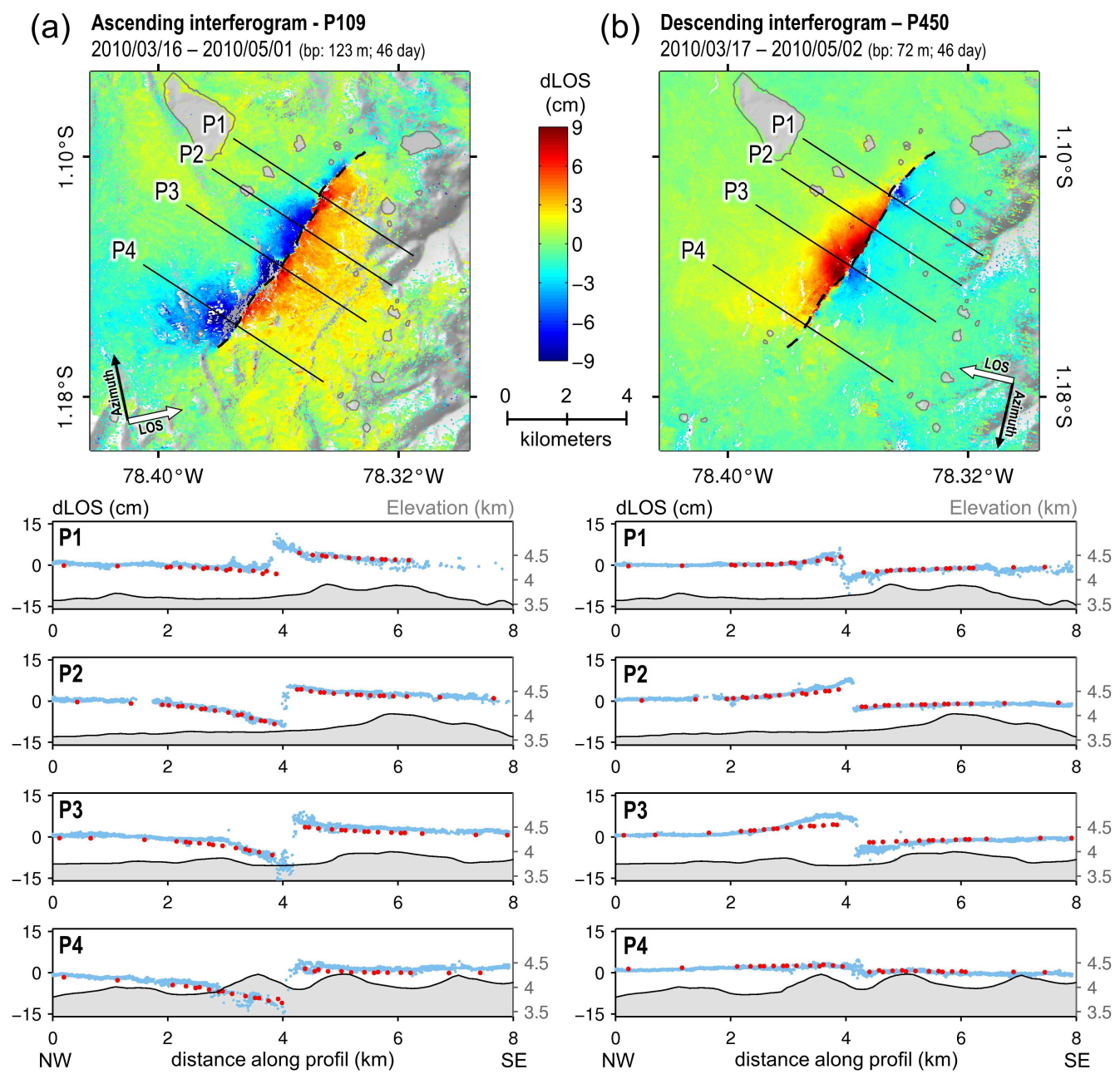
(a)
Ascending interferogram - P109
2010/03/16 – 2010/05/01 (bp: 123 m; 46 day)
(b)
Descending interferogram – P450
2010/03/17 – 2010/05/02 (bp: 72 m; 46 day)
dLOS (cm)
9
6
3
0
−3
−6
−9
P1
P2
P3
P4
1.10°S
1.18°S
78.40°W
78.32°W
Azimuth
LOS
0
2
4
kilometers
dLOS (cm)
Elevation (km)
distance along profil (km)
NW
SE

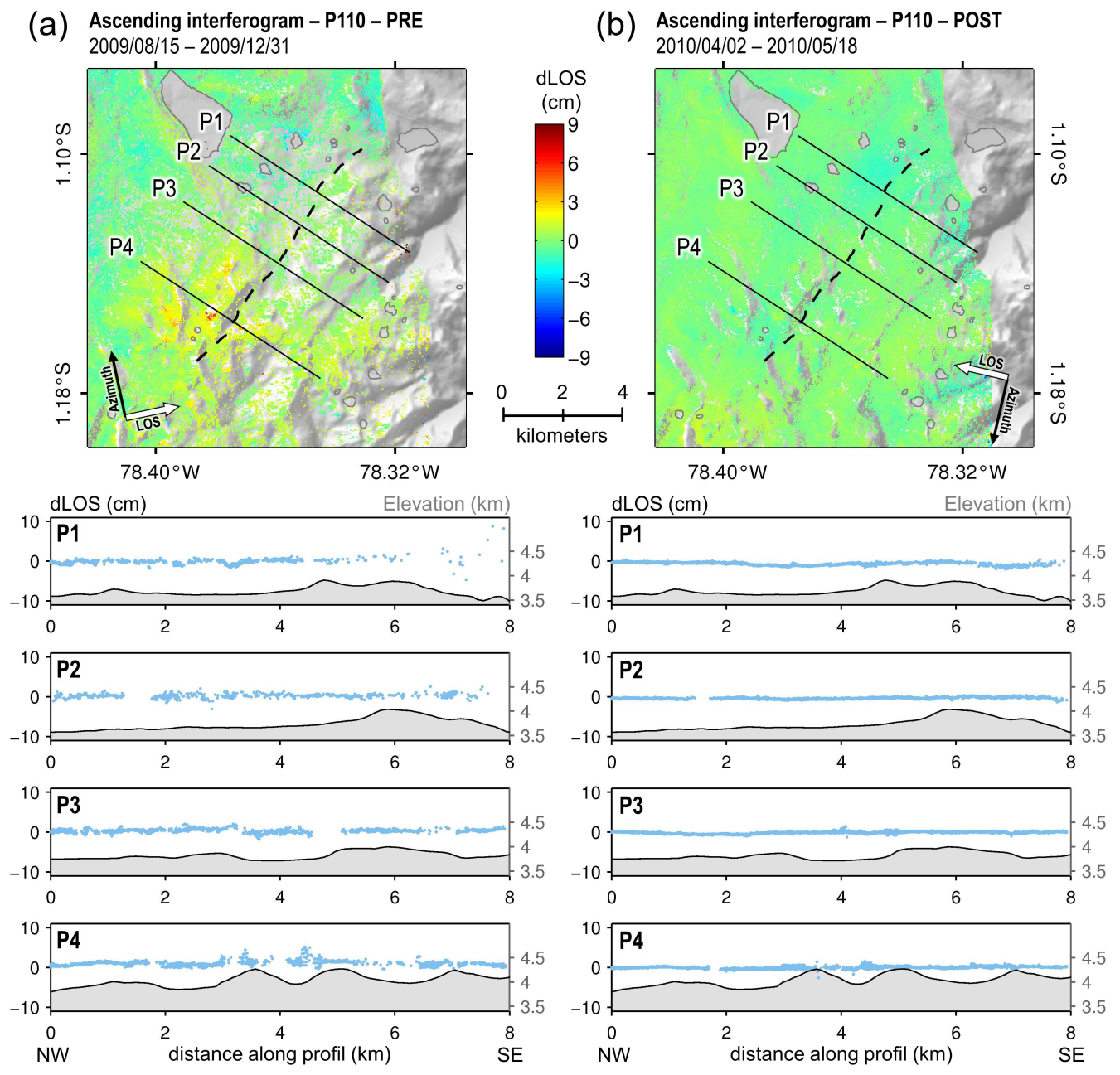
(a)
Ascending interferogram – P110 – PRE
2009/08/15 – 2009/12/31
(b)
Ascending interferogram – P110 – POST
2010/04/02 – 2010/05/18
dLOS (cm)
9
6
3
0
−3
−6
−9
P1
P2
P3
P4
1.10°S
1.18°S
78.40°W
78.32°W
Azimuth
LOS
0
2
4
kilometers
dLOS (cm)
Elevation (km)
distance along profil (km)
NW
SE

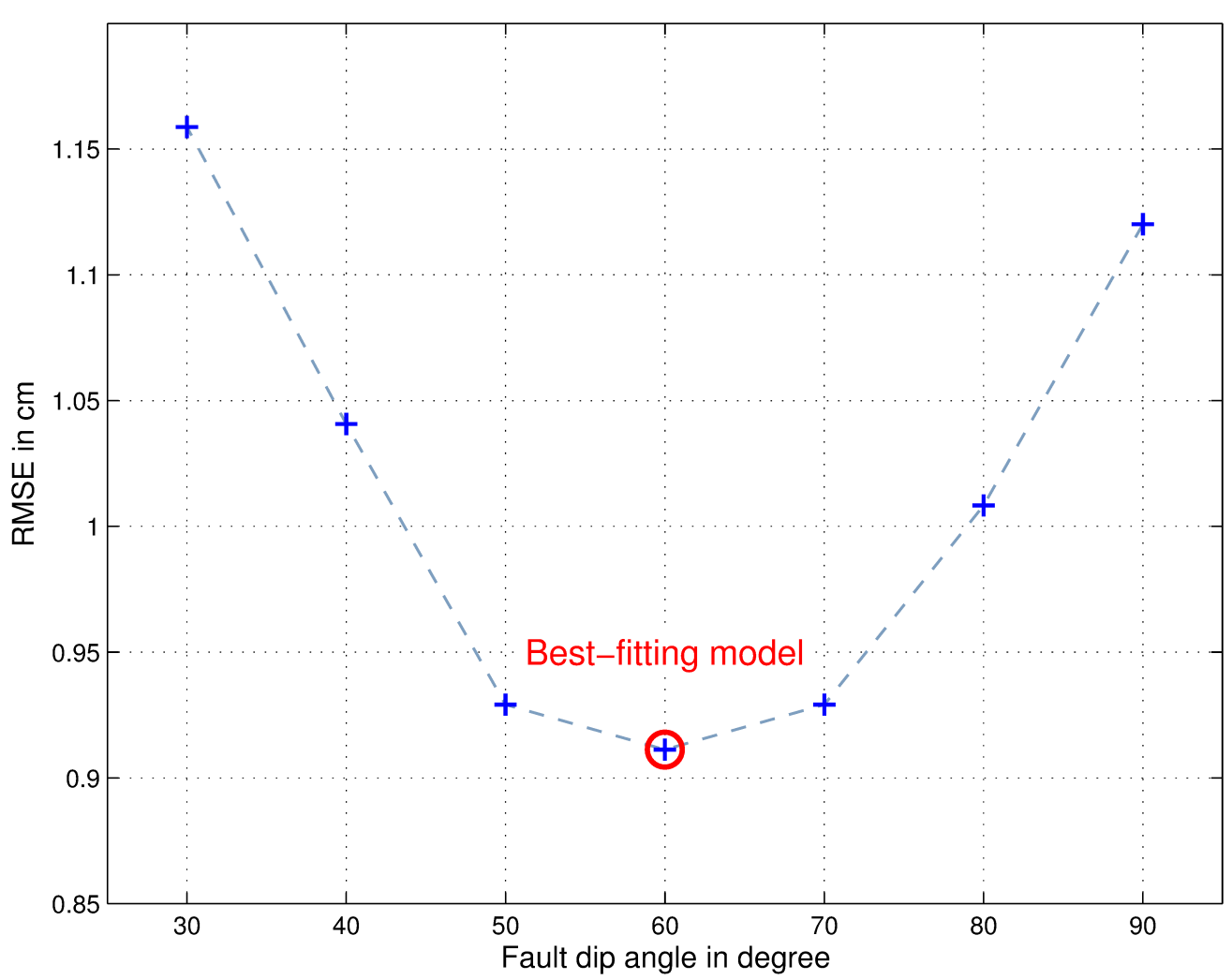
RMSE in cm
1.15
1.1
1.05
1
0.95
0.9
0.85
Best−fitting model
30
40
50
60
70
80
90
Fault dip angle in degree

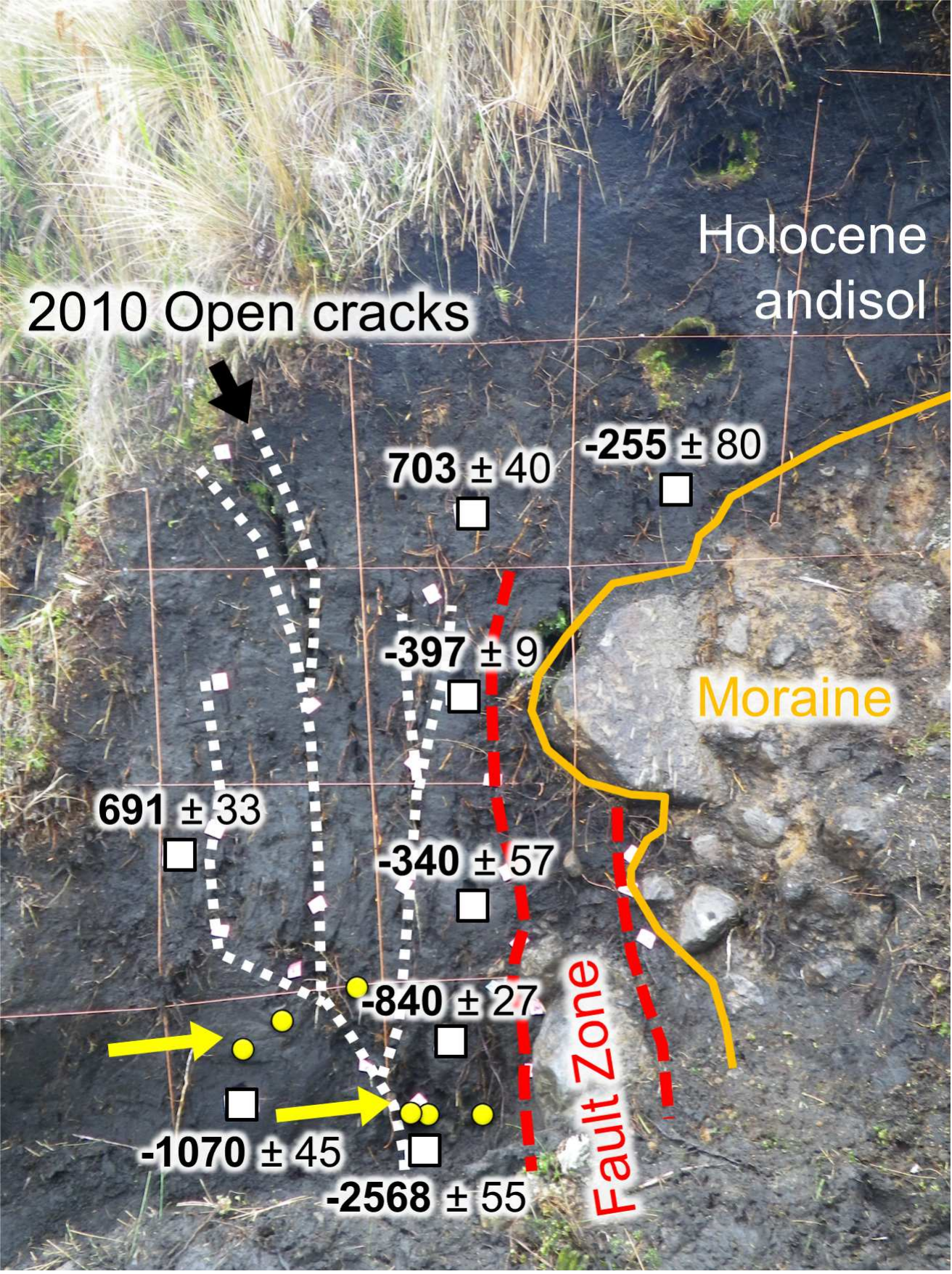
Holocene
andisol
2010 Open cracks
703 ± 40
-255 ± 80
-397 ± 9
Moraine
691 ± 33
-340 ± 57
-840 ± 27
Fault Zone
-1070 ± 45
-2568 ± 55

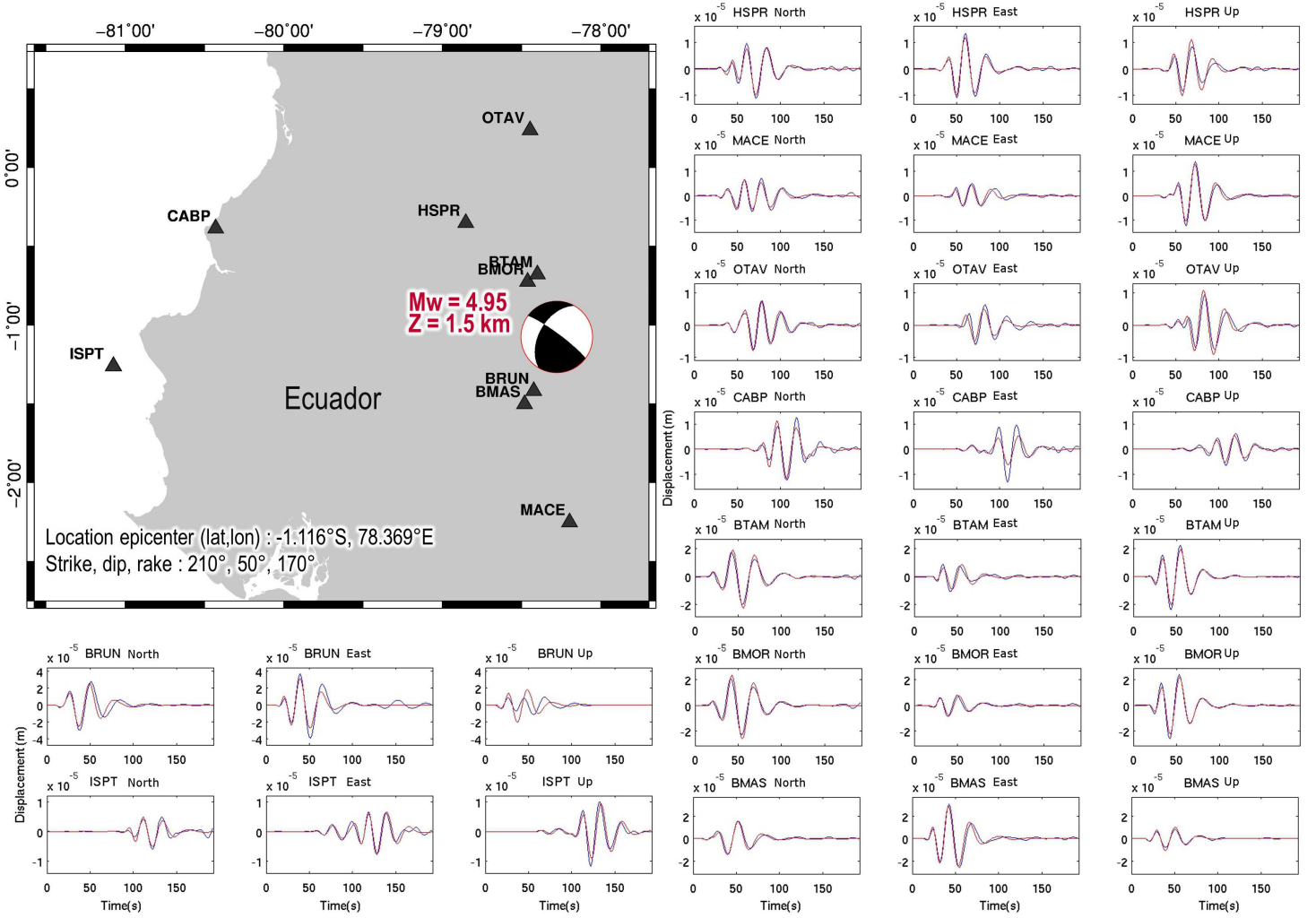
−81°00'
−80°00'
−79°00'
−78°00'
0°00'
−1°00'
−2°00'
OTAV
CABP
HSPR
BTAM
BMOR
Mw = 4.95
Z = 1.5 km
ISPT
BRUN
BMAS
Ecuador
MACE
Location epicenter (lat,lon) : -1.116°S, 78.369°E
Strike, dip, rake : 210°, 50°, 170°
HSPR North
HSPR East
HSPR Up
MACE North
MACE East
MACE Up
OTAV North
OTAV East
OTAV Up
CABP North
CABP East
CABP Up
BTAM North
BTAM East
BTAM Up
BMOR North
BMOR East
BMOR Up
BRUN North
BRUN East
BRUN Up
ISPT North
ISPT East
ISPT Up
BMAS North
BMAS East
BMAS Up
Displacement (m)
Time(s)

slip_(cm)	rake_angle	Lon1	Lon2	Lon3	Lat1	Lat2	Lat3
1.4174	0	7.94e+05	7.9239e+05	7.9267e+05	9.8821e+06	9.8799e+06	9.883e+06
1.46	0	7.9267e+05	7.9239e+05	7.9095e+05	9.883e+06	9.8799e+06	9.8806e+06
1.5459	0	7.8923e+05	7.9095e+05	7.905e+05	9.8781e+06	9.8806e+06	9.8773e+06
1.4276	0	7.905e+05	7.9095e+05	7.9239e+05	9.8773e+06	9.8806e+06	9.8799e+06
0.29293	343.9	7.8814e+05	7.8867e+05	7.9012e+05	9.8716e+06	9.8746e+06	9.8743e+06
0.51945	180	7.9012e+05	7.905e+05	7.9186e+05	9.8743e+06	9.8773e+06	9.8766e+06
0.5039	357.28	7.8867e+05	7.905e+05	7.9012e+05	9.8746e+06	9.8773e+06	9.8743e+06
0.97571	357.66	7.8698e+05	7.8867e+05	7.8814e+05	9.8724e+06	9.8746e+06	9.8716e+06
1.4913	0	7.8751e+05	7.8698e+05	7.8579e+05	9.8757e+06	9.8724e+06	9.8732e+06
1.4315	359.86	7.8867e+05	7.8698e+05	7.8751e+05	9.8746e+06	9.8724e+06	9.8757e+06
1.518	0	7.8923e+05	7.905e+05	7.8751e+05	9.8781e+06	9.8773e+06	9.8757e+06
1.3071	359.95	7.8751e+05	7.905e+05	7.8867e+05	9.8757e+06	9.8773e+06	9.8746e+06
0.30439	0	7.9186e+05	7.905e+05	7.9292e+05	9.8766e+06	9.8773e+06	9.8785e+06
1.0408	0	7.9292e+05	7.905e+05	7.9239e+05	9.8785e+06	9.8773e+06	9.8799e+06
0.10021	0	7.9186e+05	7.9292e+05	7.9337e+05	9.8766e+06	9.8785e+06	9.8772e+06
0.53471	0	7.9337e+05	7.9292e+05	7.9399e+05	9.8772e+06	9.8785e+06	9.8786e+06
1.1551	-187.51	7.8814e+05	7.9012e+05	7.8991e+05	9.8716e+06	9.8743e+06	9.8723e+06
2.6879	-180.11	7.9173e+05	7.9012e+05	7.9186e+05	9.8748e+06	9.8743e+06	9.8766e+06
0.19253	0	7.942e+05	7.9337e+05	7.9399e+05	9.8777e+06	9.8772e+06	9.8786e+06
0.56044	180	7.942e+05	7.9391e+05	7.9337e+05	9.8777e+06	9.8769e+06	9.8772e+06
0.9618	0	7.9577e+05	7.9493e+05	7.9504e+05	9.8809e+06	9.8797e+06	9.8814e+06
1.1089	0	7.9504e+05	7.9493e+05	7.94e+05	9.8814e+06	9.8797e+06	9.88e+06
1.1681	0	7.94e+05	7.9292e+05	7.9239e+05	9.88e+06	9.8785e+06	9.8799e+06
0.96584	0	7.9399e+05	7.9292e+05	7.94e+05	9.8786e+06	9.8785e+06	9.88e+06
0.95748	0	7.94e+05	7.9493e+05	7.9399e+05	9.88e+06	9.8797e+06	9.8786e+06
1.2423	0	7.94e+05	7.94e+05	7.9504e+05	9.88e+06	9.8821e+06	9.8814e+06
1.3183	0	7.9239e+05	7.94e+05	7.94e+05	9.8799e+06	9.8821e+06	9.88e+06
0.37549	-197.14	7.8814e+05	7.8991e+05	7.8902e+05	9.8716e+06	9.8723e+06	9.871e+06
3.8758	-182.75	7.9094e+05	7.8991e+05	7.9012e+05	9.8735e+06	9.8723e+06	9.8743e+06
5.2069	-180.73	7.9012e+05	7.9173e+05	7.9094e+05	9.8743e+06	9.8748e+06	9.8735e+06
0.67935	180	7.9337e+05	7.9391e+05	7.934e+05	9.8772e+06	9.8769e+06	9.8764e+06
1.8037	180	7.931e+05	7.934e+05	7.937e+05	9.8756e+06	9.8764e+06	9.8761e+06
1.6185	180	7.937e+05	7.934e+05	7.9391e+05	9.8761e+06	9.8764e+06	9.8769e+06
0.49098	0	7.9575e+05	7.9549e+05	7.9493e+05	9.8799e+06	9.8792e+06	9.8797e+06
0.59655	0	7.9575e+05	7.9577e+05	7.963e+05	9.8799e+06	9.8809e+06	9.8805e+06
0.74253	0	7.9493e+05	7.9577e+05	7.9575e+05	9.8797e+06	9.8809e+06	9.8799e+06
0.56175	0	7.9399e+05	7.9493e+05	7.9483e+05	9.8786e+06	9.8797e+06	9.8787e+06
0.27413	0	7.9493e+05	7.9549e+05	7.9483e+05	9.8797e+06	9.8792e+06	9.8787e+06
0.86089	180	7.9475e+05	7.942e+05	7.9483e+05	9.878e+06	9.8777e+06	9.8787e+06
0.11332	0	7.9483e+05	7.942e+05	7.9399e+05	9.8787e+06	9.8777e+06	9.8786e+06
8.0958	180	7.9173e+05	7.9255e+05	7.9225e+05	9.8748e+06	9.875e+06	9.8743e+06
9.3876	-188.06	7.9635e+05	7.9631e+05	7.961e+05	9.8782e+06	9.8778e+06	9.8778e+06
0.69295	316.8	7.9666e+05	7.97e+05	7.9655e+05	9.8803e+06	9.88e+06	9.8794e+06
1.8812	-191.81	7.9619e+05	7.958e+05	7.9655e+05	9.8788e+06	9.8789e+06	9.8794e+06
34.109	-180.65	7.9494e+05	7.9501e+05	7.9471e+05	9.8761e+06	9.8759e+06	9.8758e+06
34.465	-181.07	7.9522e+05	7.9501e+05	7.9494e+05	9.8762e+06	9.8759e+06	9.8761e+06
4.5965	180	7.9267e+05	7.9255e+05	7.9173e+05	9.8759e+06	9.875e+06	9.8748e+06
0.80652	180	7.9337e+05	7.934e+05	7.9267e+05	9.8772e+06	9.8764e+06	9.8759e+06
3.6565	180	7.931e+05	7.9255e+05	7.9267e+05	9.8756e+06	9.875e+06	9.8759e+06
1.7116	180	7.9267e+05	7.934e+05	7.931e+05	9.8759e+06	9.8764e+06	9.8756e+06
0.91061	180	7.9186e+05	7.9337e+05	7.9267e+05	9.8766e+06	9.8772e+06	9.8759e+06
2.5823	180	7.9267e+05	7.9173e+05	7.9186e+05	9.8759e+06	9.8748e+06	9.8766e+06

9.4084	-185.01	7.9532e+05	7.9479e+05	7.9507e+05	9.8774e+06	9.877e+06	9.8777e+06
16.637	-183.2	7.9535e+05	7.9502e+05	7.9532e+05	9.8771e+06	9.8768e+06	9.8774e+06
14.269	-183.93	7.9532e+05	7.9502e+05	7.9479e+05	9.8774e+06	9.8768e+06	9.877e+06
1.9364	180	7.9447e+05	7.942e+05	7.9475e+05	9.8773e+06	9.8777e+06	9.878e+06
1.9103	180	7.9391e+05	7.942e+05	7.9447e+05	9.8769e+06	9.8777e+06	9.8773e+06
3.6335	-181.44	7.9475e+05	7.9507e+05	7.9447e+05	9.878e+06	9.8777e+06	9.8773e+06
6.6134	-182.96	7.9507e+05	7.9479e+05	7.9447e+05	9.8777e+06	9.877e+06	9.8773e+06
7.5194	-188.03	7.9567e+05	7.9532e+05	7.9507e+05	9.8782e+06	9.8774e+06	9.8777e+06
5.1754	-194.71	7.9567e+05	7.9619e+05	7.9613e+05	9.8782e+06	9.8788e+06	9.8783e+06
3.1927	-190.95	7.958e+05	7.9619e+05	7.9567e+05	9.8789e+06	9.8788e+06	9.8782e+06
2.8804	-182.35	7.9528e+05	7.9507e+05	7.9475e+05	9.8784e+06	9.8777e+06	9.878e+06
1.131	-182.51	7.9549e+05	7.958e+05	7.9528e+05	9.8792e+06	9.8789e+06	9.8784e+06
4.2388	-186.14	7.9528e+05	7.9567e+05	7.9507e+05	9.8784e+06	9.8782e+06	9.8777e+06
2.7314	-186.44	7.958e+05	7.9567e+05	7.9528e+05	9.8789e+06	9.8782e+06	9.8784e+06
1.2747	180	7.9475e+05	7.9483e+05	7.9528e+05	9.878e+06	9.8787e+06	9.8784e+06
0.57252	180	7.9528e+05	7.9483e+05	7.9549e+05	9.8784e+06	9.8787e+06	9.8792e+06
1.7344	0	7.9055e+05	7.9012e+05	7.8979e+05	9.8708e+06	9.8702e+06	9.8704e+06
13.529	-181.67	7.9164e+05	7.9109e+05	7.9136e+05	9.8728e+06	9.8723e+06	9.873e+06
9.1852	180	7.929e+05	7.9225e+05	7.9255e+05	9.8748e+06	9.8743e+06	9.875e+06
5.629	180	7.929e+05	7.9255e+05	7.931e+05	9.8748e+06	9.875e+06	9.8756e+06
5.406	-197.39	7.9672e+05	7.9635e+05	7.9663e+05	9.8784e+06	9.8782e+06	9.8786e+06
7.1095	-191.54	7.9651e+05	7.9635e+05	7.9672e+05	9.8781e+06	9.8782e+06	9.8784e+06
8.5199	-189.03	7.9631e+05	7.9635e+05	7.9651e+05	9.8778e+06	9.8782e+06	9.8781e+06
10.601	180	7.9587e+05	7.9586e+05	7.9609e+05	9.8771e+06	9.8775e+06	9.8775e+06
9.7992	-183.76	7.961e+05	7.9631e+05	7.9609e+05	9.8778e+06	9.8778e+06	9.8775e+06
10.146	-182.31	7.9609e+05	7.9586e+05	7.961e+05	9.8775e+06	9.8775e+06	9.8778e+06
0.22778	0	7.963e+05	7.9666e+05	7.9613e+05	9.8805e+06	9.8803e+06	9.8796e+06
0.38775	0	7.9613e+05	7.9575e+05	7.963e+05	9.8796e+06	9.8799e+06	9.8805e+06
0.21026	0	7.9549e+05	7.9575e+05	7.9613e+05	9.8792e+06	9.8799e+06	9.8796e+06
0.45733	180	7.9613e+05	7.958e+05	7.9549e+05	9.8796e+06	9.8789e+06	9.8792e+06
0.70366	-183.47	7.9655e+05	7.958e+05	7.9613e+05	9.8794e+06	9.8789e+06	9.8796e+06
0.065215	304.57	7.9613e+05	7.9666e+05	7.9655e+05	9.8796e+06	9.8803e+06	9.8794e+06
2.1055	309.39	7.97e+05	7.9725e+05	7.9696e+05	9.88e+06	9.8798e+06	9.8795e+06
1.4168	310.93	7.9655e+05	7.97e+05	7.9696e+05	9.8794e+06	9.88e+06	9.8795e+06
1.5192	298.65	7.9696e+05	7.9687e+05	7.9655e+05	9.8795e+06	9.8792e+06	9.8794e+06
28.842	180	7.9449e+05	7.9457e+05	7.9425e+05	9.8755e+06	9.8753e+06	9.8752e+06
17.557	180	7.9356e+05	7.9397e+05	7.9379e+05	9.875e+06	9.8752e+06	9.8748e+06
3.5409	180	7.931e+05	7.937e+05	7.9344e+05	9.8756e+06	9.8761e+06	9.8754e+06
5.1678	180	7.9344e+05	7.929e+05	7.931e+05	9.8754e+06	9.8748e+06	9.8756e+06
8.1498	180	7.9356e+05	7.929e+05	7.9344e+05	9.875e+06	9.8748e+06	9.8754e+06
33.47	-180.11	7.9479e+05	7.9471e+05	7.9501e+05	9.8756e+06	9.8758e+06	9.8759e+06
30.727	180	7.9479e+05	7.9457e+05	7.9449e+05	9.8756e+06	9.8753e+06	9.8755e+06
31.661	180	7.9449e+05	7.9471e+05	7.9479e+05	9.8755e+06	9.8758e+06	9.8756e+06
25.555	180	7.9449e+05	7.9425e+05	7.9422e+05	9.8755e+06	9.8752e+06	9.8755e+06
22.564	180	7.9422e+05	7.9425e+05	7.9397e+05	9.8755e+06	9.8752e+06	9.8752e+06
35.554	180	7.9264e+05	7.9286e+05	7.9257e+05	9.873e+06	9.8728e+06	9.8727e+06
36.458	-180.01	7.9257e+05	7.9233e+05	7.9264e+05	9.8727e+06	9.8728e+06	9.873e+06
32.865	180	7.9288e+05	7.9286e+05	7.9264e+05	9.8732e+06	9.8728e+06	9.873e+06
24.301	180	7.9314e+05	7.9302e+05	7.9274e+05	9.874e+06	9.8737e+06	9.8737e+06
35.463	180	7.9264e+05	7.9233e+05	7.9252e+05	9.873e+06	9.8728e+06	9.8732e+06
22.511	180	7.9331e+05	7.9314e+05	7.9341e+05	9.8738e+06	9.874e+06	9.8742e+06
23.356	180	7.9302e+05	7.9314e+05	7.9331e+05	9.8737e+06	9.874e+06	9.8738e+06
30.814	-180.81	7.9544e+05	7.9522e+05	7.9516e+05	9.8765e+06	9.8762e+06	9.8764e+06

33.506	-181.47		7.9516e+05	7.9522e+05	7.9494e+05	9.8764e+06	9.8762e+06	9.8761e+06
26.814		180	7.9516e+05	7.9544e+05	7.9544e+05	9.8764e+06	9.8768e+06	9.8765e+06
21.506		180	7.9544e+05	7.9544e+05	7.9565e+05	9.8765e+06	9.8768e+06	9.8768e+06
11.444	-180.35		7.9564e+05	7.9586e+05	7.9587e+05	9.8771e+06	9.8775e+06	9.8771e+06
13.419		180	7.9587e+05	7.9565e+05	7.9564e+05	9.8771e+06	9.8768e+06	9.8771e+06
16.535		180	7.9564e+05	7.9565e+05	7.9544e+05	9.8771e+06	9.8768e+06	9.8768e+06
17.065	-180.04		7.9564e+05	7.9544e+05	7.9535e+05	9.8771e+06	9.8768e+06	9.8771e+06
21.817		180	7.9535e+05	7.9544e+05	7.9521e+05	9.8771e+06	9.8768e+06	9.8767e+06
21.449	-181.44		7.9521e+05	7.9502e+05	7.9535e+05	9.8767e+06	9.8768e+06	9.8771e+06
26.325		180	7.9544e+05	7.9516e+05	7.9521e+05	9.8768e+06	9.8764e+06	9.8767e+06
9.164	-190.83		7.9532e+05	7.9567e+05	7.9575e+05	9.8774e+06	9.8782e+06	9.8777e+06
10.227	-187.75		7.961e+05	7.9586e+05	7.9575e+05	9.8778e+06	9.8775e+06	9.8777e+06
7.6739	-180.1		7.9178e+05	7.9171e+05	7.92e+05	9.8713e+06	9.8716e+06	9.8716e+06
0.81363		0	7.9099e+05	7.9127e+05	7.9104e+05	9.8709e+06	9.8709e+06	9.8706e+06
3.899		180	7.9144e+05	7.9171e+05	7.9151e+05	9.8715e+06	9.8716e+06	9.8712e+06
1.1036		180	7.9157e+05	7.9127e+05	7.9151e+05	9.871e+06	9.8709e+06	9.8712e+06
2.7728		180	7.9151e+05	7.9178e+05	7.9157e+05	9.8712e+06	9.8713e+06	9.871e+06
4.5536		180	7.9171e+05	7.9178e+05	7.9151e+05	9.8716e+06	9.8713e+06	9.8712e+06
0.38045		180	7.9134e+05	7.9127e+05	7.9157e+05	9.8707e+06	9.8709e+06	9.871e+06
0.56408	359.05		7.9134e+05	7.9113e+05	7.9104e+05	9.8707e+06	9.8704e+06	9.8706e+06
0.34435		0	7.9104e+05	7.9127e+05	7.9134e+05	9.8706e+06	9.8709e+06	9.8707e+06
6.8023	-181.72		7.9142e+05	7.9079e+05	7.9109e+05	9.872e+06	9.8716e+06	9.8723e+06
19.851	-183.04		7.9142e+05	7.9164e+05	7.9193e+05	9.872e+06	9.8728e+06	9.8726e+06
13.477	-182.57		7.9109e+05	7.9164e+05	7.9142e+05	9.8723e+06	9.8728e+06	9.872e+06
1.5477		0	7.902e+05	7.8979e+05	7.8948e+05	9.8711e+06	9.8704e+06	9.8706e+06
1.5321		0	7.9055e+05	7.8979e+05	7.902e+05	9.8708e+06	9.8704e+06	9.8711e+06
0.39686		0	7.902e+05	7.9079e+05	7.9055e+05	9.8711e+06	9.8716e+06	9.8708e+06
10.94	-180.47		7.9136e+05	7.9094e+05	7.9169e+05	9.873e+06	9.8735e+06	9.8738e+06
9.0632	-180.17		7.9169e+05	7.9094e+05	7.9173e+05	9.8738e+06	9.8735e+06	9.8748e+06
10.684		180	7.9173e+05	7.9225e+05	7.9169e+05	9.8748e+06	9.8743e+06	9.8738e+06
14.498		180	7.9195e+05	7.9169e+05	7.9225e+05	9.8735e+06	9.8738e+06	9.8743e+06
17.136	-180.63		7.9195e+05	7.9164e+05	7.9136e+05	9.8735e+06	9.8728e+06	9.873e+06
14.514	-180.22		7.9136e+05	7.9169e+05	7.9195e+05	9.873e+06	9.8738e+06	9.8735e+06
21.978		180	7.9309e+05	7.9314e+05	7.9274e+05	9.8744e+06	9.874e+06	9.8737e+06
12.844		180	7.9309e+05	7.929e+05	7.9356e+05	9.8744e+06	9.8748e+06	9.875e+06
20.737		180	7.9341e+05	7.9314e+05	7.9309e+05	9.8742e+06	9.874e+06	9.8744e+06
3.8517	-209.65		7.9672e+05	7.9663e+05	7.9694e+05	9.8784e+06	9.8786e+06	9.8787e+06
6.0294	-196.5		7.9641e+05	7.9635e+05	7.9613e+05	9.8786e+06	9.8782e+06	9.8783e+06
5.1022	-198.38		7.9641e+05	7.9663e+05	7.9635e+05	9.8786e+06	9.8786e+06	9.8782e+06
4.9575	-196.38		7.9613e+05	7.9619e+05	7.9641e+05	9.8783e+06	9.8788e+06	9.8786e+06
3.159	299.87		7.9715e+05	7.9709e+05	7.9737e+05	9.879e+06	9.8792e+06	9.8793e+06
28.532		180	7.9436e+05	7.9425e+05	7.9457e+05	9.875e+06	9.8752e+06	9.8753e+06
17.851		180	7.9356e+05	7.9379e+05	7.935e+05	9.875e+06	9.8748e+06	9.8746e+06
16.039		180	7.935e+05	7.9309e+05	7.9356e+05	9.8746e+06	9.8744e+06	9.875e+06
19.068		180	7.9341e+05	7.9309e+05	7.935e+05	9.8742e+06	9.8744e+06	9.8746e+06
21.772		180	7.935e+05	7.9373e+05	7.9341e+05	9.8746e+06	9.8745e+06	9.8742e+06
21.048		180	7.9379e+05	7.9373e+05	7.935e+05	9.8748e+06	9.8745e+06	9.8746e+06
16.535	-183.34		7.9479e+05	7.9502e+05	7.9455e+05	9.877e+06	9.8768e+06	9.8763e+06
36.156	-180.53		7.9264e+05	7.9257e+05	7.9286e+05	9.8725e+06	9.8727e+06	9.8728e+06
30.306		180	7.9286e+05	7.9288e+05	7.9307e+05	9.8728e+06	9.8732e+06	9.8732e+06
24.545		180	7.9309e+05	7.9331e+05	7.9329e+05	9.8735e+06	9.8738e+06	9.8735e+06
24.547		180	7.9302e+05	7.9331e+05	7.9309e+05	9.8737e+06	9.8738e+06	9.8735e+06
25.78		180	7.9329e+05	7.9307e+05	7.9309e+05	9.8735e+06	9.8732e+06	9.8735e+06

28.053		180	7.9309e+05	7.9307e+05	7.9288e+05	9.8735e+06	9.8732e+06	9.8732e+06
27.145		180	7.9302e+05	7.9309e+05	7.9281e+05	9.8737e+06	9.8735e+06	9.8734e+06
29.153		180	7.9281e+05	7.9309e+05	7.9288e+05	9.8734e+06	9.8735e+06	9.8732e+06
27.935		180	7.9274e+05	7.9302e+05	7.9281e+05	9.8737e+06	9.8737e+06	9.8734e+06
31.689		180	7.9281e+05	7.9252e+05	7.9274e+05	9.8734e+06	9.8732e+06	9.8737e+06
32.277		180	7.9281e+05	7.9288e+05	7.9264e+05	9.8734e+06	9.8732e+06	9.873e+06
33.842		180	7.9264e+05	7.9252e+05	7.9281e+05	9.873e+06	9.8732e+06	9.8734e+06
25.362	-180.02		7.9329e+05	7.9331e+05	7.9351e+05	9.8735e+06	9.8738e+06	9.8738e+06
11.816	-183.61		7.9586e+05	7.9564e+05	7.9559e+05	9.8775e+06	9.8771e+06	9.8774e+06
11.013	-187.34		7.9559e+05	7.9575e+05	7.9586e+05	9.8774e+06	9.8777e+06	9.8775e+06
13.951	-182.55		7.9559e+05	7.9564e+05	7.9535e+05	9.8774e+06	9.8771e+06	9.8771e+06
13.863	-184.7		7.9535e+05	7.9532e+05	7.9559e+05	9.8771e+06	9.8774e+06	9.8774e+06
11.283	-188.12		7.9532e+05	7.9575e+05	7.9559e+05	9.8774e+06	9.8777e+06	9.8774e+06
7.3003	-195.1		7.9601e+05	7.9567e+05	7.9613e+05	9.878e+06	9.8782e+06	9.8783e+06
8.7437	-193.58		7.9601e+05	7.9575e+05	7.9567e+05	9.878e+06	9.8777e+06	9.8782e+06
9.4947	-192.14		7.961e+05	7.9575e+05	7.9601e+05	9.8778e+06	9.8777e+06	9.878e+06
7.6558	-195.06		7.9613e+05	7.9635e+05	7.9601e+05	9.8783e+06	9.8782e+06	9.878e+06
9.0868	-192.38		7.9601e+05	7.9635e+05	7.961e+05	9.878e+06	9.8782e+06	9.8778e+06
26.544	-183.68		7.9221e+05	7.9214e+05	7.9243e+05	9.8719e+06	9.8722e+06	9.8722e+06
11.13	-181.51		7.92e+05	7.9171e+05	7.9193e+05	9.8716e+06	9.8716e+06	9.8719e+06
16.117	-183.04		7.9193e+05	7.9221e+05	7.92e+05	9.8719e+06	9.8719e+06	9.8716e+06
21.337	-184.13		7.9214e+05	7.9221e+05	7.9193e+05	9.8722e+06	9.8719e+06	9.8719e+06
21.045	-184.8		7.9214e+05	7.9193e+05	7.9186e+05	9.8722e+06	9.8719e+06	9.8721e+06
20.273	-184.37		7.9186e+05	7.9142e+05	7.9193e+05	9.8721e+06	9.872e+06	9.8726e+06
31.226	-183.2		7.9243e+05	7.9214e+05	7.9236e+05	9.8722e+06	9.8722e+06	9.8725e+06
34.14	-182.13		7.9236e+05	7.9264e+05	7.9243e+05	9.8725e+06	9.8725e+06	9.8722e+06
36.161	-181.11		7.9257e+05	7.9264e+05	7.9236e+05	9.8727e+06	9.8725e+06	9.8725e+06
36.182	-180.85		7.9233e+05	7.9257e+05	7.9236e+05	9.8728e+06	9.8727e+06	9.8725e+06
0.35782	353.44		7.9055e+05	7.9092e+05	7.9071e+05	9.8699e+06	9.8701e+06	9.8698e+06
3.5255	-180.05		7.9106e+05	7.9142e+05	7.9144e+05	9.8714e+06	9.872e+06	9.8715e+06
3.1749		180	7.9079e+05	7.9142e+05	7.9106e+05	9.8716e+06	9.872e+06	9.8714e+06
0.31772		180	7.9055e+05	7.9079e+05	7.9106e+05	9.8708e+06	9.8716e+06	9.8714e+06
0.76839		0	7.9106e+05	7.9099e+05	7.9055e+05	9.8714e+06	9.8709e+06	9.8708e+06
0.48058		0	7.9127e+05	7.9099e+05	7.9126e+05	9.8709e+06	9.8709e+06	9.8712e+06
0.44322		180	7.9126e+05	7.9151e+05	7.9127e+05	9.8712e+06	9.8712e+06	9.8709e+06
1.4458		180	7.9144e+05	7.9151e+05	7.9126e+05	9.8715e+06	9.8712e+06	9.8712e+06
1.1249		180	7.9126e+05	7.9106e+05	7.9144e+05	9.8712e+06	9.8714e+06	9.8715e+06
0.36394		0	7.9099e+05	7.9106e+05	7.9126e+05	9.8709e+06	9.8714e+06	9.8712e+06
1.1171		0	7.899e+05	7.902e+05	7.8948e+05	9.8714e+06	9.8711e+06	9.8706e+06
0.82397	358.79		7.8948e+05	7.8902e+05	7.899e+05	9.8706e+06	9.871e+06	9.8714e+06
0.11496	325.37		7.899e+05	7.8902e+05	7.8991e+05	9.8714e+06	9.871e+06	9.8723e+06
17.404		180	7.9252e+05	7.9195e+05	7.9225e+05	9.874e+06	9.8735e+06	9.8743e+06
21.378		180	7.9252e+05	7.9309e+05	7.9274e+05	9.874e+06	9.8744e+06	9.8737e+06
14.242		180	7.9225e+05	7.929e+05	7.9252e+05	9.8743e+06	9.8748e+06	9.874e+06
16.017		180	7.929e+05	7.9309e+05	7.9252e+05	9.8748e+06	9.8744e+06	9.874e+06
31.183		180	7.9274e+05	7.9252e+05	7.9222e+05	9.8737e+06	9.8732e+06	9.8732e+06
25.662		180	7.9222e+05	7.9252e+05	7.9274e+05	9.8732e+06	9.874e+06	9.8737e+06
22.375		180	7.9195e+05	7.9252e+05	7.9222e+05	9.8735e+06	9.874e+06	9.8732e+06
22.12	-180.52		7.9164e+05	7.9195e+05	7.9222e+05	9.8728e+06	9.8735e+06	9.8732e+06
24.913	-181.42		7.9193e+05	7.9164e+05	7.9222e+05	9.8726e+06	9.8728e+06	9.8732e+06
30.725	-181.09		7.9222e+05	7.9233e+05	7.9193e+05	9.8732e+06	9.8728e+06	9.8726e+06
33.458	-180.09		7.9222e+05	7.9252e+05	7.9233e+05	9.8732e+06	9.8732e+06	9.8728e+06
2.4324	-265.23		7.9715e+05	7.9694e+05	7.9685e+05	9.879e+06	9.8787e+06	9.8789e+06

2.6955	290.62		7.9685e+05	7.9709e+05	7.9715e+05	9.8789e+06	9.8792e+06	9.879e+06
2.6827	-232.81		7.9685e+05	7.9694e+05	7.9663e+05	9.8789e+06	9.8787e+06	9.8786e+06
2.3384	291.33		7.9687e+05	7.9709e+05	7.9685e+05	9.8792e+06	9.8792e+06	9.8789e+06
3.3498	302.86		7.9718e+05	7.9737e+05	7.9709e+05	9.8795e+06	9.8793e+06	9.8792e+06
2.7089	306.66		7.9718e+05	7.9696e+05	7.9725e+05	9.8795e+06	9.8795e+06	9.8798e+06
2.7716	302.98		7.9718e+05	7.9709e+05	7.9687e+05	9.8795e+06	9.8792e+06	9.8792e+06
2.3965	305.92		7.9687e+05	7.9696e+05	7.9718e+05	9.8792e+06	9.8795e+06	9.8795e+06
23.624		180	7.9402e+05	7.9373e+05	7.9379e+05	9.8748e+06	9.8745e+06	9.8748e+06
27.95		180	7.9415e+05	7.9393e+05	7.9402e+05	9.8747e+06	9.8744e+06	9.8748e+06
27.384		180	7.9402e+05	7.9393e+05	7.9373e+05	9.8748e+06	9.8744e+06	9.8745e+06
28.011		180	7.9402e+05	7.9436e+05	7.9415e+05	9.8748e+06	9.875e+06	9.8747e+06
27.264		180	7.9425e+05	7.9436e+05	7.9402e+05	9.8752e+06	9.875e+06	9.8748e+06
23.871		180	7.9397e+05	7.9425e+05	7.9402e+05	9.8752e+06	9.8752e+06	9.8748e+06
21.651		180	7.9402e+05	7.9379e+05	7.9397e+05	9.8748e+06	9.8748e+06	9.8752e+06
25.391	-180.11		7.9341e+05	7.9373e+05	7.9358e+05	9.8742e+06	9.8745e+06	9.8741e+06
24.791	-180.24		7.9358e+05	7.9331e+05	7.9341e+05	9.8741e+06	9.8738e+06	9.8742e+06
29.779		180	7.9358e+05	7.9393e+05	7.9372e+05	9.8741e+06	9.8744e+06	9.8741e+06
28.565		180	7.9373e+05	7.9393e+05	7.9358e+05	9.8745e+06	9.8744e+06	9.8741e+06
29.099		180	7.9372e+05	7.9351e+05	7.9358e+05	9.8741e+06	9.8738e+06	9.8741e+06
26.656	-180.31		7.9358e+05	7.9351e+05	7.9331e+05	9.8741e+06	9.8738e+06	9.8738e+06
28.807	-180.23		7.9443e+05	7.9471e+05	7.9449e+05	9.8758e+06	9.8758e+06	9.8755e+06
24.962		180	7.9449e+05	7.9422e+05	7.9443e+05	9.8755e+06	9.8755e+06	9.8758e+06
11.804	-182.09		7.9479e+05	7.9455e+05	7.9422e+05	9.877e+06	9.8763e+06	9.8765e+06
7.2564	-181.77		7.9422e+05	7.9447e+05	7.9479e+05	9.8765e+06	9.8773e+06	9.877e+06
3.6181		180	7.9422e+05	7.937e+05	7.9391e+05	9.8765e+06	9.8761e+06	9.8769e+06
3.9662	-180.44		7.9391e+05	7.9447e+05	7.9422e+05	9.8769e+06	9.8773e+06	9.8765e+06
6.9035	-181.54		7.9166e+05	7.9171e+05	7.9144e+05	9.8718e+06	9.8716e+06	9.8715e+06
10.579	-182.63		7.9166e+05	7.9193e+05	7.9171e+05	9.8718e+06	9.8719e+06	9.8716e+06
14.977	-184.64		7.9166e+05	7.9186e+05	7.9193e+05	9.8718e+06	9.8721e+06	9.8719e+06
7.695	-182.79		7.9144e+05	7.9142e+05	7.9166e+05	9.8715e+06	9.872e+06	9.8718e+06
14.069	-184.64		7.9142e+05	7.9186e+05	7.9166e+05	9.872e+06	9.8721e+06	9.8718e+06
26.621	-184.35		7.9214e+05	7.9186e+05	7.9213e+05	9.8722e+06	9.8721e+06	9.8724e+06
31.124	-183.34		7.9213e+05	7.9236e+05	7.9214e+05	9.8724e+06	9.8725e+06	9.8722e+06
33.571	-182.1		7.9233e+05	7.9236e+05	7.9213e+05	9.8728e+06	9.8725e+06	9.8724e+06
31.027	-182.36		7.9193e+05	7.9233e+05	7.9213e+05	9.8726e+06	9.8728e+06	9.8724e+06
26.443	-183.96		7.9213e+05	7.9186e+05	7.9193e+05	9.8724e+06	9.8721e+06	9.8726e+06
0.65466		0	7.9078e+05	7.9055e+05	7.9037e+05	9.8702e+06	9.8699e+06	9.87e+06
0.41547	359.16		7.9092e+05	7.9055e+05	7.9078e+05	9.8701e+06	9.8699e+06	9.8702e+06
0.61296		0	7.9113e+05	7.9092e+05	7.9078e+05	9.8704e+06	9.8701e+06	9.8702e+06
0.81748		0	7.9104e+05	7.9113e+05	7.9078e+05	9.8706e+06	9.8704e+06	9.8702e+06
9.3998	-181.91		7.9136e+05	7.9109e+05	7.9077e+05	9.873e+06	9.8723e+06	9.8725e+06
8.6806	-181.58		7.9077e+05	7.9094e+05	7.9136e+05	9.8725e+06	9.8735e+06	9.873e+06
5.4724	-182.59		7.8991e+05	7.9094e+05	7.9077e+05	9.8723e+06	9.8735e+06	9.8725e+06
1.0256	-180.49		7.9079e+05	7.902e+05	7.9047e+05	9.8716e+06	9.8711e+06	9.8718e+06
0.020924	-216.93		7.902e+05	7.899e+05	7.9047e+05	9.8711e+06	9.8714e+06	9.8718e+06
4.3387	-181.55		7.9109e+05	7.9079e+05	7.9047e+05	9.8723e+06	9.8716e+06	9.8718e+06
5.8079	-182.21		7.9047e+05	7.9077e+05	7.9109e+05	9.8718e+06	9.8725e+06	9.8723e+06
1.0515	-185.19		7.9047e+05	7.899e+05	7.8991e+05	9.8718e+06	9.8714e+06	9.8723e+06
3.9772	-183.04		7.8991e+05	7.9077e+05	7.9047e+05	9.8723e+06	9.8725e+06	9.8718e+06
1.719	-258.86		7.9687e+05	7.9685e+05	7.9659e+05	9.8792e+06	9.8789e+06	9.8789e+06
3.5173	-199.72		7.9659e+05	7.9641e+05	7.9619e+05	9.8789e+06	9.8786e+06	9.8788e+06
3.6277	-204.56		7.9663e+05	7.9641e+05	7.9659e+05	9.8786e+06	9.8786e+06	9.8789e+06
2.4623	-226.68		7.9659e+05	7.9685e+05	7.9663e+05	9.8789e+06	9.8789e+06	9.8786e+06

1.2618	-250.99		7.9655e+05	7.9687e+05	7.9659e+05	9.8794e+06	9.8792e+06	9.8789e+06
2.0005	-204.17		7.9659e+05	7.9619e+05	7.9655e+05	9.8789e+06	9.8788e+06	9.8794e+06
3.6661	299.97		7.9759e+05	7.9737e+05	7.9743e+05	9.8796e+06	9.8793e+06	9.8797e+06
3.6141	300.89		7.9737e+05	7.9718e+05	7.9743e+05	9.8793e+06	9.8795e+06	9.8797e+06
3.281	303.05		7.9743e+05	7.9718e+05	7.9725e+05	9.8797e+06	9.8795e+06	9.8798e+06
31.926	-181.43		7.9494e+05	7.9471e+05	7.947e+05	9.8761e+06	9.8758e+06	9.8761e+06
28.92	-181.12		7.9471e+05	7.9443e+05	7.947e+05	9.8758e+06	9.8758e+06	9.8761e+06
25.043	-181.64		7.947e+05	7.9443e+05	7.9455e+05	9.8761e+06	9.8758e+06	9.8763e+06
18.992	-180.6		7.9455e+05	7.9443e+05	7.9402e+05	9.8763e+06	9.8758e+06	9.8757e+06
6.5436		180	7.937e+05	7.9422e+05	7.9402e+05	9.8761e+06	9.8765e+06	9.8757e+06
12.087	-180.58		7.9402e+05	7.9422e+05	7.9455e+05	9.8757e+06	9.8765e+06	9.8763e+06
5.5227		180	7.9402e+05	7.9344e+05	7.937e+05	9.8757e+06	9.8754e+06	9.8761e+06
20.584		180	7.9402e+05	7.9443e+05	7.9422e+05	9.8757e+06	9.8758e+06	9.8755e+06
18.718		180	7.9402e+05	7.9422e+05	7.9397e+05	9.8757e+06	9.8755e+06	9.8752e+06
14.317		180	7.9402e+05	7.9397e+05	7.9356e+05	9.8757e+06	9.8752e+06	9.875e+06
8.5685		180	7.9356e+05	7.9344e+05	7.9402e+05	9.875e+06	9.8754e+06	9.8757e+06
1.0669		0	7.9054e+05	7.9078e+05	7.9037e+05	9.8703e+06	9.8702e+06	9.87e+06
1.3678		0	7.9054e+05	7.9037e+05	7.9012e+05	9.8703e+06	9.87e+06	9.8702e+06
1.6558		0	7.9054e+05	7.9012e+05	7.9055e+05	9.8703e+06	9.8702e+06	9.8708e+06
23.156	-182.89		7.9492e+05	7.9455e+05	7.9502e+05	9.8764e+06	9.8763e+06	9.8768e+06
26.79	-182.63		7.9492e+05	7.947e+05	7.9455e+05	9.8764e+06	9.8761e+06	9.8763e+06
24.933	-181.93		7.9502e+05	7.9521e+05	7.9492e+05	9.8768e+06	9.8767e+06	9.8764e+06
28.517	-181.32		7.9492e+05	7.9521e+05	7.9516e+05	9.8764e+06	9.8767e+06	9.8764e+06
31.926	-181.98		7.9492e+05	7.9516e+05	7.9494e+05	9.8764e+06	9.8764e+06	9.8761e+06
30.904	-182.31		7.9494e+05	7.947e+05	7.9492e+05	9.8761e+06	9.8761e+06	9.8764e+06
1.1878		0	7.9104e+05	7.9078e+05	7.9079e+05	9.8706e+06	9.8702e+06	9.8706e+06
1.3077		0	7.9078e+05	7.9054e+05	7.9079e+05	9.8702e+06	9.8703e+06	9.8706e+06
1.2453		0	7.9079e+05	7.9099e+05	7.9104e+05	9.8706e+06	9.8709e+06	9.8706e+06
1.3684		0	7.9055e+05	7.9099e+05	7.9079e+05	9.8708e+06	9.8709e+06	9.8706e+06
1.5516		0	7.9079e+05	7.9054e+05	7.9055e+05	9.8706e+06	9.8703e+06	9.8708e+06

z1	z2	z3
7591.8	7654	10392
10392	7654	10392
10392	10392	7768.9
7768.9	10392	7654
5428.8	7709.6	5339
5339	7768.9	5151.9
7709.6	7768.9	5339
7875.5	7709.6	5428.8
10392	7875.5	10392
7709.6	7875.5	10392
10392	7768.9	10392
10392	7768.9	7709.6
5151.9	7768.9	5551.1
5551.1	7768.9	7654
5151.9	5551.1	3640.7
3640.7	5551.1	4097.9
5428.8	5339	3677.2
3492.4	5339	5151.9
2943.9	3640.7	4097.9
2943.9	2496	3640.7
3855.2	3901.9	5391.9
5391.9	3901.9	5489.9
5489.9	5551.1	7654
4097.9	5551.1	5489.9
5489.9	3901.9	4097.9
5489.9	7591.8	5391.9
7654	7591.8	5489.9
5428.8	3677.2	3566.5
3327.8	3677.2	5339
5339	3492.4	3327.8
3640.7	2496	2718.7
2338.9	2718.7	2010.1
2010.1	2718.7	2496
2896.5	2557.8	3901.9
2896.5	3855.2	2723.2
3901.9	3855.2	2896.5
4097.9	3901.9	2986.6
3901.9	2557.8	2986.6
2399.8	2943.9	2986.6
2986.6	2943.9	4097.9
3492.4	2582.1	2322.1
366.32	0	333.48
1960.2	1251.9	1304.8
1204.2	1816.3	1304.8
316.24	0	330.69
0	0	316.24
3297.7	2582.1	3492.4
3640.7	2718.7	3297.7
2338.9	2582.1	3297.7
3297.7	2718.7	2338.9
5151.9	3640.7	3297.7
3297.7	3492.4	5151.9

1070.5	1394.5	1713.8
644.44	868.67	1070.5
1070.5	868.67	1394.5
2100.1	2943.9	2399.8
2496	2943.9	2100.1
2399.8	1713.8	2100.1
1713.8	1394.5	2100.1
1297.9	1070.5	1713.8
1297.9	1204.2	823.61
1816.3	1204.2	1297.9
2110.3	1713.8	2399.8
2557.8	1816.3	2110.3
2110.3	1297.9	1713.8
1816.3	1297.9	2110.3
2399.8	2986.6	2110.3
2110.3	2986.6	2557.8
1270.2	1247.4	1930.7
1635.4	1943.1	2317.1
1867.6	2322.1	2582.1
1867.6	2582.1	2338.9
0	366.32	323.27
0	366.32	0
0	366.32	0
0	336.07	0
333.48	0	0
0	336.07	333.48
2723.2	1960.2	2056.7
2056.7	2896.5	2723.2
2557.8	2896.5	2056.7
2056.7	1816.3	2557.8
1304.8	1816.3	2056.7
2056.7	1960.2	1304.8
1251.9	709.01	837.42
1304.8	1251.9	837.42
837.42	638.7	1304.8
343.42	0	340.11
1158.8	733.38	642.81
2338.9	2010.1	1702.8
1702.8	1867.6	2338.9
1158.8	1867.6	1702.8
0	330.69	0
0	0	343.42
343.42	330.69	0
343.42	340.11	678.69
678.69	340.11	733.38
460.38	0	299.96
299.96	688.91	460.38
278.28	0	460.38
756.77	595.39	1025.9
460.38	688.91	808.7
351.51	756.77	585.86
595.39	756.77	351.51
0	0	290.25

290.25	0	316.24
290.25	291.67	0
0	291.67	0
317.97	336.07	0
0	0	317.97
317.97	0	291.67
317.97	291.67	644.44
644.44	291.67	485.69
485.69	868.67	644.44
291.67	290.25	485.69
1070.5	1297.9	741.67
333.48	336.07	741.67
0	335.89	0
715.7	327.36	332.17
707.54	335.89	326.32
0	327.36	326.32
326.32	0	0
335.89	0	326.32
0	327.36	0
0	0	332.17
332.17	327.36	0
1209.1	1664.7	1943.1
1209.1	1635.4	1043.9
1943.1	1635.4	1209.1
2012.2	1930.7	2586.9
1270.2	1930.7	2012.2
2012.2	1664.7	1270.2
2317.1	3327.8	2617.7
2617.7	3327.8	3492.4
3492.4	2322.1	2617.7
1959.5	2617.7	2322.1
1959.5	1635.4	2317.1
2317.1	2617.7	1959.5
1193.4	756.77	1025.9
1193.4	1867.6	1158.8
585.86	756.77	1193.4
0	323.27	0
643.44	366.32	823.61
643.44	323.27	366.32
823.61	1204.2	643.44
0	291.56	0
0	340.11	0
1158.8	642.81	787.34
787.34	1193.4	1158.8
585.86	1193.4	787.34
787.34	387.08	585.86
642.81	387.08	787.34
1394.5	868.67	1060.2
0	299.96	0
0	278.28	0
298.07	351.51	0
595.39	351.51	298.07
0	0	298.07

298.07	0	278.28
595.39	298.07	592.5
592.5	298.07	278.28
1025.9	595.39	592.5
592.5	808.7	1025.9
592.5	278.28	460.38
460.38	808.7	592.5
0	351.51	0
336.07	317.97	620.18
620.18	741.67	336.07
620.18	317.97	644.44
644.44	1070.5	620.18
1070.5	741.67	620.18
677.73	1297.9	823.61
677.73	741.67	1297.9
333.48	741.67	677.73
823.61	366.32	677.73
677.73	366.32	333.48
0	329.77	0
0	335.89	338.25
338.25	0	0
329.77	0	338.25
329.77	338.25	710.2
710.2	1209.1	1043.9
0	329.77	329.25
329.25	0	0
299.96	0	329.25
688.91	299.96	329.25
329.08	0	0
1063	1209.1	707.54
1664.7	1209.1	1063
1270.2	1664.7	1063
1063	715.7	1270.2
327.36	715.7	612.65
612.65	326.32	327.36
707.54	326.32	612.65
612.65	1063	707.54
715.7	1063	612.65
2728.8	2012.2	2586.9
2586.9	3566.5	2728.8
2728.8	3566.5	3677.2
1630.5	1959.5	2322.1
1630.5	1193.4	1025.9
2322.1	1867.6	1630.5
1867.6	1193.4	1630.5
1025.9	808.7	1287.5
1287.5	1630.5	1025.9
1959.5	1630.5	1287.5
1635.4	1959.5	1287.5
1043.9	1635.4	1287.5
1287.5	688.91	1043.9
1287.5	808.7	688.91
0	0	343.62

343.62	291.56	0
343.62	0	323.27
638.7	291.56	343.62
447.3	0	291.56
447.3	837.42	709.01
447.3	291.56	638.7
638.7	837.42	447.3
319.24	387.08	642.81
0	0	319.24
319.24	0	387.08
319.24	0	0
340.11	0	319.24
733.38	340.11	319.24
319.24	642.81	733.38
585.86	387.08	257.97
257.97	351.51	585.86
257.97	0	0
387.08	0	257.97
0	0	257.97
257.97	0	351.51
720.71	330.69	343.42
343.42	678.69	720.71
1394.5	1060.2	1713.5
1713.5	2100.1	1394.5
1713.5	2010.1	2496
2496	2100.1	1713.5
668.06	335.89	707.54
668.06	338.25	335.89
668.06	710.2	338.25
707.54	1209.1	668.06
1209.1	710.2	668.06
329.77	710.2	616.33
616.33	329.25	329.77
688.91	329.25	616.33
1043.9	688.91	616.33
616.33	710.2	1043.9
370.61	329.08	705.3
0	329.08	370.61
0	0	370.61
332.17	0	370.61
2317.1	1943.1	2651.7
2651.7	3327.8	2317.1
3677.2	3327.8	2651.7
1664.7	2012.2	2394.7
2012.2	2728.8	2394.7
1943.1	1664.7	2394.7
2394.7	2651.7	1943.1
2394.7	2728.8	3677.2
3677.2	2651.7	2394.7
638.7	343.62	750.23
750.23	643.44	1204.2
323.27	643.44	750.23
750.23	343.62	323.27

1304.8	638.7	750.23
750.23	1204.2	1304.8
0	0	340.48
0	447.3	340.48
340.48	447.3	709.01
316.24	330.69	617.62
330.69	720.71	617.62
617.62	720.71	1060.2
1060.2	720.71	1237.2
2010.1	1713.5	1237.2
1237.2	1713.5	1060.2
1237.2	1702.8	2010.1
1237.2	720.71	678.69
1237.2	678.69	733.38
1237.2	733.38	1158.8
1158.8	1702.8	1237.2
804.18	370.61	705.3
804.18	705.3	1247.4
804.18	1247.4	1270.2
638.79	1060.2	868.67
638.79	617.62	1060.2
868.67	485.69	638.79
638.79	485.69	290.25
638.79	290.25	316.24
316.24	617.62	638.79
332.17	370.61	674.61
370.61	804.18	674.61
674.61	715.7	332.17
1270.2	715.7	674.61
674.61	804.18	1270.2